1

The F Ring of Saturn

C. D. MURRAY & R. S. FRENCH

Located 3,500 km beyond the main ring system, the unusual, time-varying structure of the F ring of Saturn has continued to challenge ring dynamicists since its discovery by the Pioneer 11 spacecraft in 1979. Data from the two Voyager flybys revealed a far from uniform, narrow ring with extensive azimuthal structure and a multi-stranded appearance. With the arrival of the Cassini spacecraft in 2004 came the opportunity to study the ring and its variability in detail for the duration of the mission. The picture that has emerged is of a dynamic ring that is subjected to the gravitational influence of the adjacent satellites Prometheus and Pandora as well as the collisional effects of a population of smaller objects orbiting close to the ring's core. Here we show how spacecraft observations and modelling have combined to provide a more detailed understanding of the key processes involved in shaping this most enigmatic of rings.

Figure 1.1 Discovery image of the F ring obtained by the IPP experiment onboard the Pioneer 11 spacecraft. The image has been enhanced to show the detection of the ring at the top right of the frame. Image courtesy of NASA Ames Research Center, Pioneer Imaging Photopolarimeter.

1.1 Pre-Cassini observations of the F ring

Saturn's F ring was first detected in observations made by the Imaging Photopolarimeter (IPP) experiment on the Pioneer 11 spacecraft when it passed Saturn in 1979 (Gehrels et al., 1980). Located at 2.33 Saturn radii (R_S), it was described as a narrow feature < 800 km wide with an optical depth $\tau < 2 \times 10^{-3}$ and indications of "clumpiness" – although, as pointed out by Cuzzi and Burns (1988), the main rings had a similar appearance in the discovery image (see Figure 1.1), probably due to the high noise level. The first indication of the unusual nature of the ring was obtained from measurements of the charged particle environment by Simpson et al. (1980). The inbound and outbound fluxes of the 7-17 MeV electrons showed absorption features that did not match, indicative of the presence of orbiting material in the region of the F ring.

New opportunities to observe the F ring came with the flybys of Saturn by the Voyager 1 and 2 spacecraft in November 1980 and August 1981, respectively. Data from the Imaging Science Subsystem (ISS) instrument on Voyager 1 provided the first resolved images of the ring. Initial observations described by Smith et al. (1981) showed an eccentric ring with three strands, each ~ 20 km in width, which appeared to be parallel at some longitudes but with two intersecting strands at others. Figure 1.2 shows the twisted appearance of the ring along with apparent kinks, knots and clumps at various longitudes. Bright clumps were tracked from image to image and shown to move at the expected Keplerian rate of the F ring (Smith et al., 1981). The Voyager cameras also revealed the presence of two satellites, 1980 S 26 (now named Pandora) and 1980 S 27 (now named Prometheus), moving in eccentric orbits just outside and inside the orbital location of the F ring; a possible connection between the observed structure of the ring and the presence of the two satellites was immediately made (Smith et al., 1981). It was also noted that the ring, and the clumps within it, became brighter at high solar phase angles, implying the presence of a large dust component, and that the average size of the particles was estimated to be several tenths of a micrometer. The Pioneer 11 charged particle data was re-examined by Cuzzi and Burns (1988), who deduced that the absorption features provided good evidence for a belt of moonlets occupying the region between the orbits of Prometheus and Pandora.

The arrival of the Voyager 2 spacecraft at Saturn in August 1981 offered an additional opportunity to study the unusual ring. However, the braided appearance was only evident in one region of the ring, and it was concluded that the phenomenon was either localized or time-variable (Smith et al., 1982). Five strand components – one bright and four

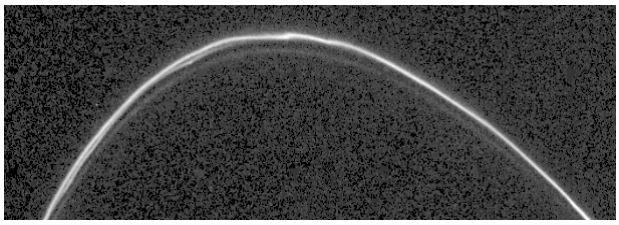

Figure 1.2 An enhanced, cropped view of a geometrically corrected image (FDS 34930.44) taken by the Voyager 1 narrow angle camera on 1980 November 12 showing the unusual structure of the F ring.

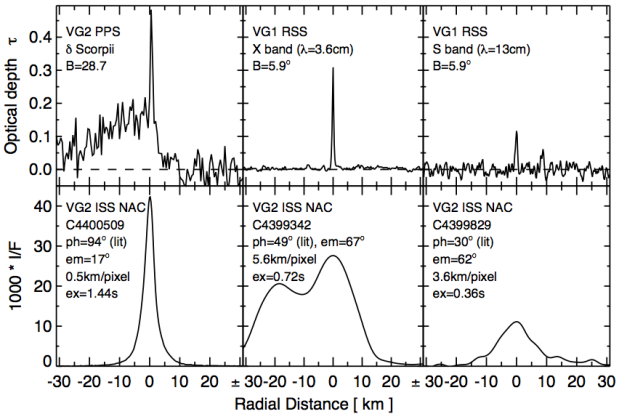

Figure 1.3 A selection of F ring core observations by Voyager. *Top:* Optical depth profiles derived from Voyager PPS and RSS occultations. *Bottom:* Normalized reflectance I/F for three selected Voyager ISS images where phase angle, emission angle, and exposure time are provided. Since RSS effectively detected particles roughly larger than wavelength λ, these observations indicate that larger particles are confined to the narrow central F ring region (Marouf et al. (1986)) (see Section 1.4.4). From Albers et al. (2012).

faint – were detected in the highest resolution images with some evidence for clumps, one of which had sharply defined edges (Smith et al., 1982). The unfortunate failure of Voyager 2's scan platform soon after ring-plane crossing meant that planned, unique observations of the F ring were lost.

The Photopolarimeter System (PPS) instrument on Voyager observed the occultation of δ Scorpii as it passed the rings on 1981 August 25, providing a resolution of ~ 100 m across the entire rings (Lane et al., 1982). The data for the F ring showed the presence of a narrow (< 3 km wide), optically thick ($\tau \sim 1$) core with evidence for ~ 10 features spread over ~ 40 km interior to the ring. Because the occultation was observed at egress only, there was no opportunity to make detections at more than one longitude and so the azimuthal extent of the observed structures remained unknown. Such a narrow core was consistent with the Voyager radio science occultation, which detected an optically thick core of width ~ 1 km (Tyler et al., 1983; Marouf et al., 1986). Figure 1.3 shows the Voyager PPS and RSS occultations in comparison to selected Voyager ISS profiles.

Following the Voyager flybys and before the arrival of the Cassini spacecraft in 2004, several authors investigated the perturbing effect of adjacent satellites on a narrow ring. Using an efficient impulse approximation, Showalter and Burns (1982) modeled the ring as a set of perturbed, non-interacting test particles and were able to produce structure reminiscent of that seen in the F ring. Kolvoord and Burns (1992) included the perturbing effects of an inclined satellite on three concentric strands in their numerical simulation thereby producing structures even more similar to those seen in the Voyager images. Giuliatti Winter (1994) and Murray (1994) studied the localized effect of Prometheus on the ring. They showed that the approach of the satellite to the ring on each orbit created a gap in the ring as well as the drawing out of streams of ring material, although the latter had not been observed in the limited Voyager coverage.

Murray et al. (1997) analyzed a set of Voyager high resolution images of the F ring. These images covered only 9.4% and 7.5% of the ring's total longitude during the Voyager 1 and 2 observations, respectively. On the basis of the limited data set they concluded that the ring could be modeled as a set of four strands with comparable eccentricities and near-aligned periapses. Using the best available post-Voyager orbits Borderies et al. (1983) showed a collision between the core and Prometheus was possible, although by assigning sufficient mass to the F ring in a secular theory Murray and Giuliatti Winter (1996) demonstrated that this outcome could be avoided.

Showalter (2004) tracked a total of 34 clumps in the Voyager images and showed that they exhibited mean motions that differed from that of the F ring. He concluded that they lay within a 100 km range of semi-major axes centered on the F ring. They seemed to change little on a timescale of 30 days, but no clump survived the nine months between the Voyager 1 and Voyager 2 encounters.

The observations by the Pioneer 11 and Voyager spacecraft showed a ring with many unique and puzzling features. These include the ring's narrowness, multi-stranded appearance, clumps, kinks, apparent braiding, and the fact that it has a satellite orbiting on either side of it. The Voyager-derived semi-major axis of 140185 ± 30 km (Synnott et al., 1983) could place the ring in the Roche zone (Dermott et al., 1979), and therefore there should be competition between accretion and tidal disruption at the ring's location. Numerical simulations (Showalter and Burns, 1982; Kolvoord and Burns, 1992; Giuliatti Winter, 1994) had confirmed that Prometheus, the larger and closer of the two satellites, would have a dominant perturbing effect and was capable of producing radial and azimuthal distortions. However, the limited Voyager coverage in longitude and time made it difficult to constrain models of the processes operating in the F ring. The arrival of the Cassini spacecraft at Saturn in July 2004 enabled a much more detailed study of the F ring system to be undertaken.

1.2 Cassini ISS observations of the F ring

The Cassini Imaging Science Subsystem (ISS) instrument (Porco et al., 2004) consists of a bore-sighted wide-angle camera (WAC) and narrow-angle camera (NAC) mounted on the body of the spacecraft. There were several types of dedicated observations of the F ring during the Cassini mission. By far the largest category, the ansa stare or so-called FMOVIE, consisted of taking ~ 100 successive images at one ansa, ideally for a total duration comparable to the orbital period of the ring. The individual images of the ring could be reprojected and used to create a mosaic showing the entire structure of the ring as it passed through the orbital or inertial longitude (i.e. the longitude measured with respect to a fixed direction in inertial space; see the chapter by Hedman in this book) of the ansa. Shifting the longitudes to a common epoch makes it possible to compare profiles of the ring as a function of corotating longitude.[1] As of mid-2015, ~ 130 observations of this type have been made. Some of these observations used half of the time to observe one ansa and then switched to the other side to observe the same material for the remaining half. This has the advantage of highlighting the maximum radial excursions in the ring because material that is at periapse at one ansa will be at apoapse at the other and vice versa. Other variations on the standard FMOVIE template included the use of a slow drift in inertial longitude to capture a larger range of inertial longitudes. The typical radial resolution of an FMOVIE was ~ 8 km pixel^{-1}. An FMOVIE does not give a "snapshot" of the state of the ring, partly because of the duration of the observation ($\sim$ 17 hours) but also because each piece of ring material is seen at nearly the the same longitude and (more to the point) orbital phase.

In contrast to the FMOVIEs, the ISS also executed 10 sequences of observations where Prometheus was tracked around its orbit and its interaction with the F ring was monitored. These were called streamer-channel movies, as they captured the creation of streamers of perturbed material emerging from the ring and subsequently evolving into channels a half-orbital period later. Ideally these covered 360° of inertial longitude (and orbital phase) but only a narrow range of corotating longitude. These will be discussed further in Section 1.6 below. Similar types of observations were made of other small satellites in the F ring region, and these too provided valuable coverage of the ring.

An additional type of observation was the azimuthal scan (AZSCAN), in which the cameras tracked along the ring in the decreasing longitude (i.e. anti-Keplerian) direction. This had the advantage of covering the entire ring in roughly half an orbital period although it still fell short of capturing a "snapshot" of the ring's entire structure at a single moment due to limitations on the rate at which images could be acquired. This type of observation was discontinued for operational reasons before the end of the nominal mission in 2008.

[1] The corotating longitude, λ_c, is related to the inertial longitude, λ, by the equation $\lambda_c = \lambda + (t_c - t)n$, where t_c is the chosen, fixed time (or epoch), t is the time of the observation and n is the chosen, fixed mean motion

Other F ring observations were designated as high-resolution and could involve a simple ansa stare or a longitudinal drift. In two such observations prior to 2016 the radial resolution was < 1 km pixel^{-1}. There were also observations dedicated to other ring features (e.g. the A ring edge, the Encke and Keeler gaps) that included coverage of the F ring, and almost all the astrometric images of the small satellites (the so-called SATELLORBs) also produced isolated but useful coverage of the F ring. Furthermore, several ISS sequences were designed to coincide with Cassini VIMS and UVIS observations of stellar occultations of the F ring. This enabled ISS profiles of the ring to be compared with the higher-resolution occultation profiles (see Figure 1.5).

The Cassini ISS data set includes ~ 30000 narrow angle images of the F ring at a variety of resolutions and phase angles. Details of a set of 165 dedicated sequences of F ring observations are given by Murray et al. (2017). Figure 1.4 shows a selection of officially released images of the F ring illustrating some of the types and variety of structures seen within the ring.

1.3 F ring orbit models

Synnott et al. (1981) and Synnott et al. (1983) used imaging data from the Voyager 1 and 2 encounters to calculate the orbit of the ring as well as small satellites in its vicinity. The F ring orbit was re-derived by Murray et al. (1997) based on their use of the high resolution images. However, prior to the availability of the Cassini data set, the orbit derived from occultation data by Bosh et al. (2002) (specifically fit 3 listed in table III) was the one most commonly used for planning purposes and was remarkably accurate, especially given the number of data points in the solution. It also demonstrated that, in common with a number of other eccentric rings, the F ring exhibited uniform apsidal precession. Albers et al. (2012) combined Voyager occultation data with 93 occultation detections of the F ring core from the Cassini Ultraviolet Imaging Spectrograph (UVIS) to produce the first orbit determination for the Cassini era. The main correction was to the eccentricity. Cooper et al. (2013) derived an F ring orbit from the ten ISS streamer-channel movies obtained between 2006 and 2009, each of which tracked Prometheus (and the adjacent F ring) for approximately one orbital period. The orbit derived from fitting all 9805 data points was consistent with that derived by Albers et al. (2012), apart from a difference in the longitude of periapse. The orbits derived by Bosh et al. (2002) (fit 3, Table III), Albers et al. (2012) (fit 2, Table 3) and Cooper et al. (2013) (fit 11, Table 3) are given in Table 1.1.

Cooper et al. (2013) were also able to derive individual orbits for each of the ten F ring segments that they tracked in the streamer-channel movies. They concluded that there was significant local variation in the orbital elements. For example, they found that the semi-major axis ranged from 140211.2 to 140232.0 km with typical 1σ formal errors of 0.2 km for each measurement. This implied that while it was possible to derive an averaged orbit that was consis-

Table 1.1. *Orbit determinations of the F ring*

	Bosh et al. (2002)	Albers et al. (2012)	Cooper et al. (2013)
Semi-major Axis (km)	140223.7 ± 2.0	140221.3 ± 1.8	140223.92 ± 0.09
Eccentricity ($\times 10^3$)	2.54 ± 0.05	2.35 ± 0.02	2.3636 ± 0.0004
Long. of Periapse ($^\circ$)	24.1 ± 1.6	24.2 ± 0.8	8.8 ± 0.3
Apsidal Precession Rate ($^\circ$ day^{-1})	2.7001 ± 0.0004	2.70025 ± 0.00029	2.7052 ± 0.0002
Inclination ($^\circ$ $\times 10^3$)	6.5 ± 0.7	6.43 ± 0.15	5.68 ± 0.05
Long. of Ascending Node ($^\circ$)	16.1 ± 3.6	15.0 ± 1.4	5.3 ± 0.6
Nodal Regression Rate ($^\circ$ day^{-1})	-2.6876	-2.68778	-2.6859

Notes: The epoch for all orbit determinations is J2000. The nodal regression rates for all of the orbit models were calculated from the fitted semi-major axes.

tent with that derived from the occultation data by Albers et al. (2012), there was still significant local variation to the extent the F ring has no unique semi-major axis. This has implications for any studies of resonant confinement of the ring's core.

The existence of localized structure in the F ring can be seen in the images obtained by the Cassini ISS. Figure 1.6 shows one such mosaic generated from 169 reprojected images of an FMOVIE obtained on 2007 March 17. Each individual image was pointing-corrected using background stars and then reprojected into a radius-corotating longitude frame centered on the radius calculated from the Cooper et al. (2013) ring orbit model for that longitude.

The mosaic highlights a number of features of the F ring region that have been consistently observed by Cassini during its orbital tour. The ring has a bright, non-uniform core that exhibits typical radial distortions of tens of kilometers. Measurements of the r.m.s. distortion apparent in this mosaic give a value of 23 km, which is comparable to that calculated by Murray et al. (2017) for all the 165 sequences they examined. Estimates of the full width at half maximum (FWHM) of the ring's core in this mosaic give a value of 40 km, a factor of 4 times larger than that detected in UVIS occultations (Albers et al., 2012). At the time the mosaic was obtained Prometheus had a corotating longitude of 262° and is just detectable as a short radial streak (due to the high degree of azimuthal compression in this mosaic) at this longitude with $\Delta r \approx -450$ km. A regular sequence of dark lines starting at this longitude and trailing it by $\sim 60^\circ$ can be clearly seen in Figure 1.6. This is how the streamer-channel phenomenon seen in Figure 1.4c appears in the reprojected mosaic. In Section 1.6 we show that the radial distortions are consistent with the perturbing effect of Prometheus.

On either side of the core are broader, more diffuse features that seem to emanate from the core to radial distances of ~ 400 km and are at a variety of angles to it. These "jets" of material (Murray et al., 2008) are thought to be the result of collisions between the core material and objects orbiting nearby (see Section 1.7 below for a more detailed discussion of these objects). There is also a tendency for the region where a jet meets the core to be brighter than surrounding regions; again this is indicative of a collisional process. In Figure 1.6 the narrow, near radial feature extending downwards at a corotating longitude of 30° suggests a recent collision because there has been insufficient time for Keplerian shear to take effect; in contrast, the older jets are more horizontal because the shear has had a marked effect on the particles with a range of semi-major axes contained in the jets. Given sufficient time, a particularly bright jet could shear sufficiently to form a kinematic spiral structure near the core. Such a spiral structure was identified by Charnoz et al. (2005) and an observed object, S/2004 S 6, was suggested as the putative collider. Therefore the multi-stranded F ring that had been observed since the Voyager epoch actually consists of a single core with one or more wrapped spiral structures (resulting from sheared collisional jets) on either side (Charnoz et al., 2005; Murray et al., 2008).

Figure 1.7 shows a single image from the same FMOVIE sequence used to generate the mosaic shown in Figure 1.6, together with a reprojection of the F ring part of that image. Note the approximately parallel appearance of the inner strand, even though we know from inspection of Figure 1.6 that the strand is angled to the core direction. This is consistent with the theory that the strands are simply sheared jets. The lower image highlights the non-uniform nature of the F ring's core and shows approximately six clumps that are brighter than surrounding material. These are not the same as the clumps tracked by Showalter (2004) and French et al. (2014), which were brighter, more extended features that probably correspond to collisional features in the ring. Note that the clumps are barely detectable in Figure 1.7a but are more obvious in the reprojected image of the core (Figure 1.7b).

Lam (2014) carried out an analysis of clumps detected in the core mosaics of ten FMOVIE sequences from 2006 December to 2008 January. She was able to track a total of 166 clumps from one sequence to another, thereby giving an estimate of the semi-major axis of each clump with respect to that of the F ring core. Her results are shown in Figure 1.8. The mean value is $\langle \Delta a \rangle = -2.85 \pm 5.45$ km, suggesting that there is no bias towards one side of the core or the other; the r.m.s. value was 6.13 km. In addition, 46 clumps were observed to have existed in at least three consecutive image sequences and gave a minimum clump lifetime of ~ 32 days. Of those clumps, 11 were observed to have existed for ~ 250 days. We will discuss the formation and evolution of these clumps in Section 1.6. It is important to

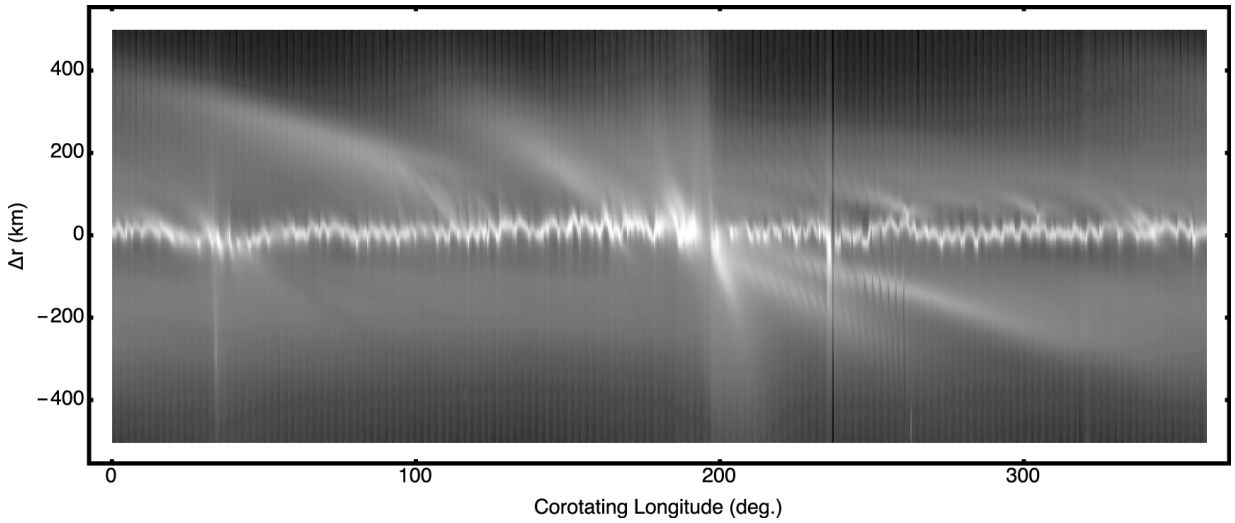

Figure 1.6 An enhanced mosaic of the F ring generated from 169 reprojected ISS NAC images obtained on 2007 March 17. $\Delta r = r_{\rm obs} - r_{\rm calc}$ is the radial displacement calculated with respect to the Cooper et al. (2013) orbit model of the F ring. The epoch of the corotating longitude is 2007 January 1 12:00 UTC using an assumed mean motion of the ring of 581.96 ° day^{-1}. An earlier version of this mosaic is shown in Figure 1e of Murray et al. (2008).

note the distinction between the localised clumps discussed here and the "extended clumps" discussed in Section 1.5 below.

All of the derived orbits shown in Table 1.1 show that the ring has an inclination of $\sim 0.006^\circ$ with respect to Saturn's equator. Though small, this is sufficient to explain the brightness asymmetry between the east and west ansae seen in the HST images taken during the 1995 ring plane crossing (Nicholson et al., 1996). The vertical structure of the ring was modeled by Scharringhausen and Nicholson (2013), who confirmed the earlier results and calculated that the F ring has a vertical FWHM of 13 ± 7 km. However, there were smaller asymmetries that could not be explained by their model and were attributed to "intrinsic longitudinal variation" in the F ring. Figure 1.9 shows two cropped Cassini images of the F ring taken a day apart. Although the F ring appears relatively flat the images show clear evidence of localized, extended vertical structure. In Figure 1.9b there is evidence for an object just beyond the F ring. It is likely that these extended features have been produced by collisions within the ring. (Collisional processes within the ring are discussed in Section 1.7 below.) Note that the longitudinal extent of the observed object is comparable to the feature shown in Figure 1.4e.

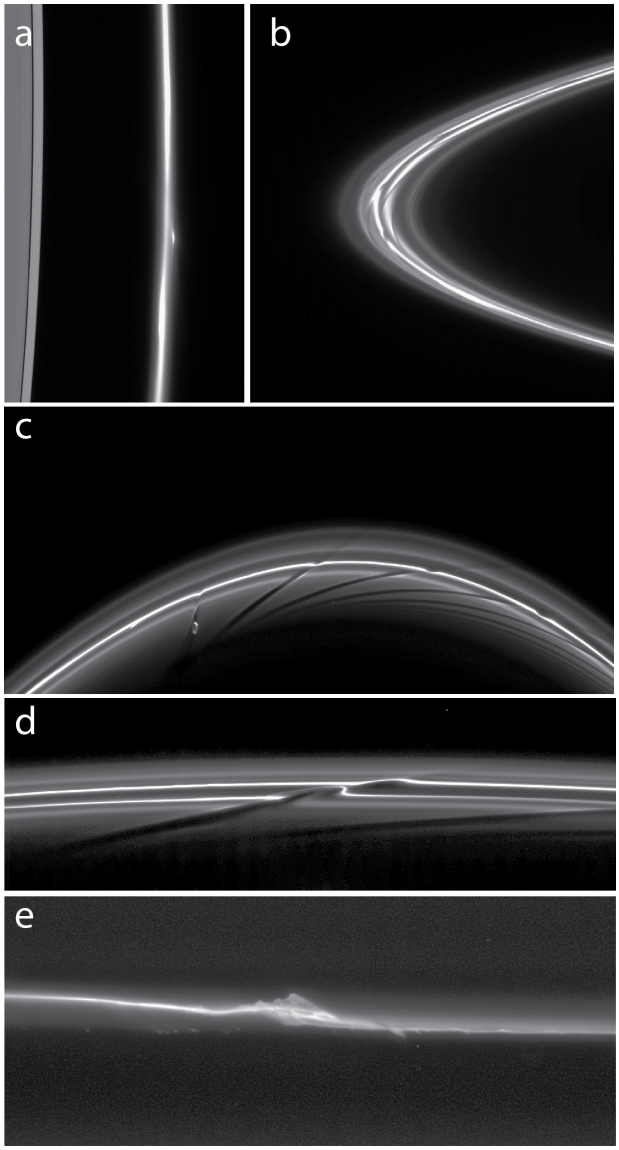

Figure 1.4 A selection of Cassini press release images of the F ring. (a) PIA08908. A NAC image (N1549830522) taken on 2007 February 10 showing the edge of the A ring (left) and $\sim 5°$ of longitude of the F ring with bright features and azimuthal structure. (b) PIA09782. A NAC image (N1571964006) taken on 2007 October 25 showing multiple strands and azimuthal structure at the F ring ansa; the image covers $\sim 18°$ of longitude. (c) PIA12684. A NAC image (N1654079744) taken on 2010 June 1 showing $\sim 17°$ of longitude of the F ring with multiple strands; the perturbing action of Prometheus (lower left) creates regular channels in the ring material interior to the bright core. (d) PIA10509. A NAC image (N1601489502) taken on 2008 September 30 showing the local effect of a recent passage by Prometheus; the image covers $\sim 4°$ of longitude at the F ring. (e) PIA08290. A high resolution NAC image (N1537898708) taken on 2006 September 25 showing irregular radial and azimuthal features in the F ring core; the image covers $\sim 0.22°$ of longitude (equivalent to ~ 530 km) of the F ring and the central feature extends ~ 35 km in radius.

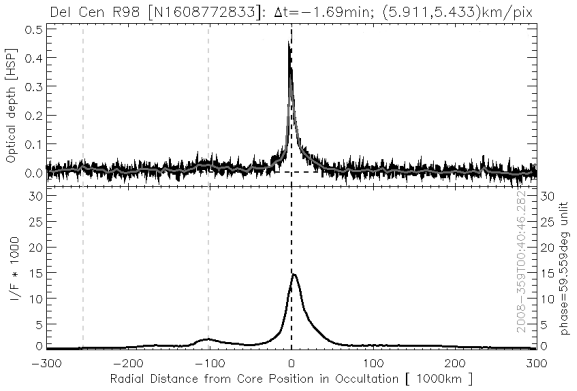

Figure 1.5 Simultaneous observation by Cassini ISS and UVIS during the stellar occultation of δ Centauri on Rev098. In the upper plot (UVIS data) the sampling data are in black and the grey line denotes the data at the same resolution as the scanned image. The lower plot is derived using data from ISS image N1608772833. (Figure from Albers (private communication))

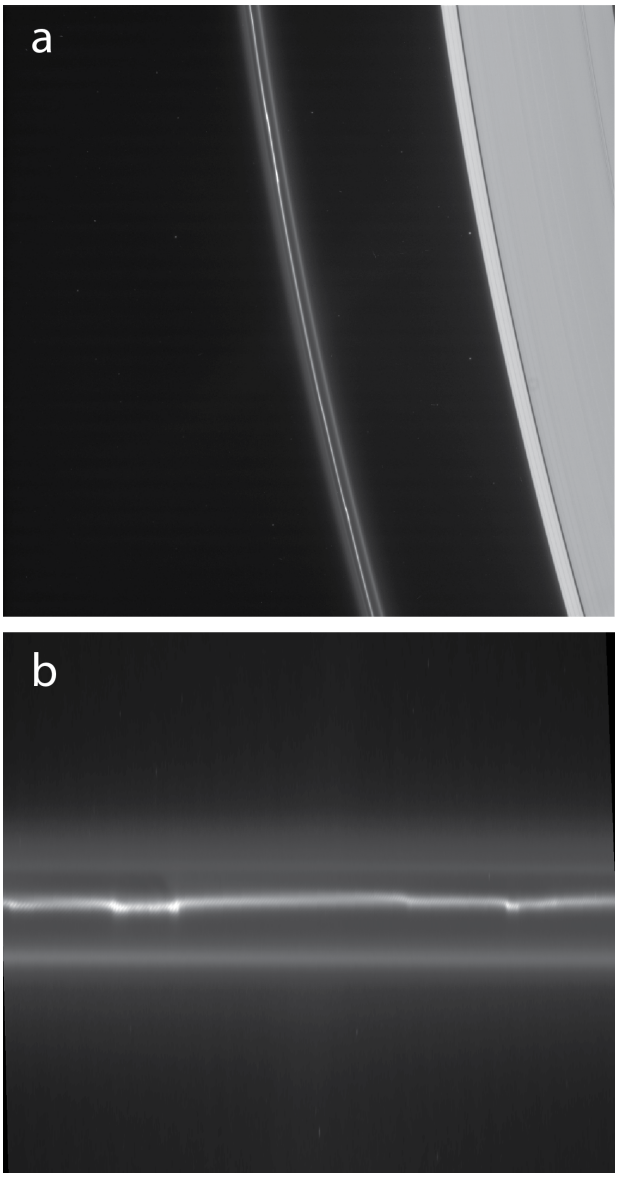

Figure 1.7 (a) Cassini NAC image N1552803087 obtained on 2007 March 17 showing a multi-stranded F ring orbiting beyond the A ring edge (right); the image covers 5.6° in longitude and was one of a sequence used to produce the mosaic shown in Figure 1.6. The radial resolution is ~ 11 km pixel^{-1}. The Keplerian motion is from top to bottom. (b) A reprojection of the F ring portion of the image shown in (a); the reprojected image extends ± 750 km on either side of the core location predicted by the model of Cooper et al. (2013). The range of corotating longitude in the system used for Figure 1.6 is from 271.58° to 277.24°.

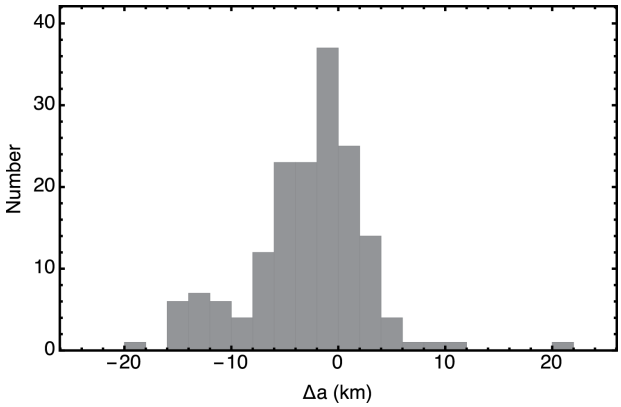

Figure 1.8 The distribution of localised clumps in semi-major axis with respect to that of the F ring core using the Cooper et al. (2013) orbit model. The data are taken from Lam (2014).

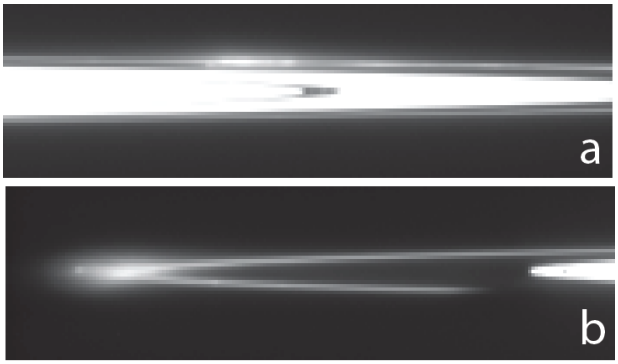

Figure 1.9 (a) A cropped Cassini NAC image N1507015271 obtained on 2005 October 3 06:52 showing a bright feature (upper center) in the F ring with vertical structure extending over ~ 0.2° in longitude. (b) A cropped Cassini NAC image N1507099722 taken on 2005 October 4 06:20 showing the same feature which has now moved to the ring ansa (left).

1.4 Photometry

1.4.1 Introduction

The interaction of electromagnetic radiation with ring particles can provide a wealth of information about particle size, shape, composition, and quantity; a thorough introduction to the physics of these interactions can be found in Cuzzi et al. (2009). Measurements fall into two main categories: scattering (usually of visible light from the Sun) and occultations (usually of stars or man-made radio sources). These measurements can be conducted at different longitudes, providing information on azimuthal variability, or across time, providing information about how the ring changes. In all cases, data must be compared to theoretical models to extract particle attributes. Unfortunately, models of scattering are often complex and computationally demanding, requiring a variety of techniques that attempt to make the problem more tractable.

1.4.2 Visible light scattering

The phase angle α, the angle between the direction to the Sun and the direction to the observer, along with particle size, shape, and composition, affects how much light from each particle is scattered in the direction of the observer. Particles that are small relative to the wavelength of light primarily scatter at high phase angles (diffraction), while particles that are large primarily scatter at lower phase angles (reflection). Measurements taken at a variety of phase angles can be combined to make a *phase curve*. This curve can then be compared with models to determine particle properties.

The amount of light scattered is also highly dependent on illumination and viewing geometry. The incidence angle i is the angle between the normal to the ring plane and the incident light source (usually the Sun) and the emission angle e is the angle between the normal to the ring plane and the observer. In the case of a ring of low optical depth, where shadowing and multi-particle obscuration can be ignored, any dependence on incidence angle disappears and emission angle can be compensated for by multiplying measurements by $\mu \equiv |\cos e|$. Although e may vary over an image, often the field of view is sufficiently narrow that a single mean emission angle is used for simplicity.

Images from Cassini and Voyager are calibrated in I/F, the ratio of the observed intensity to that produced by a perfect Lambert surface illuminated and viewed in the same geometry. In many cases the F ring is radially unresolved. Analysis is thus performed using the *equivalent width* W, a resolution-independent measurement of integrated brightness, for each radial slice. As some scattering can be present in the camera optics, it is necessary to assume that the regions far from the ring contain no material and subtract a linear- or quadratic-fit background model $B(a)$, yielding:

$$W = \int (I/F(a) - B(a))\, da, \tag{1.1}$$

The process is illustrated in Figure 1.10. Although the use of equivalent width is necessary to analyze and compare unresolved images, it has the major disadvantage that it eliminates all fine radial structure, which is a major source of information about the dynamics of the F ring. I/F is taken to be a syntactic unit, so that when analyzing a radial slice we use the notation $I/F(a)$ rather than the more technically correct $I(a)/F$.

To normalize for viewing geometry when comparing measurements of a ring of low optical depth, we compute the *normal equivalent width*:

$$W_\perp = \mu W \tag{1.2}$$

However, French et al. (2012) have shown that the F ring is sufficiently optically dense that shadowing and obscuration are important in some circumstances (see Figure 3.22 in the chapter by Cuzzi et al. for an example of the variable density of the F ring core). These can be taken into account by multiplying W instead by one of two adjustment factors (Chandrasekhar, 1960; Hansen and Travis, 1974; Dones et al., 1993),

$$Z_R(\tau, \mu, \mu_0) = \frac{\tau(\mu + \mu_0)}{\mu\mu_0(1 - \exp(-\tau(1/\mu + 1/\mu_0)))} \tag{1.3}$$

or

$$Z_T(\tau, \mu, \mu_0) = \frac{\tau(\mu - \mu_0)}{\mu\mu_0(\exp(-\tau/\mu) - \exp(-\tau/\mu_0))}, \tag{1.4}$$

depending on whether the ring was seen in reflected (Z_R) or transmitted (Z_T) light, yielding the "τ-adjusted normal equivalent width", W_τ. Here $\mu_0 \equiv |\cos i|$ and τ is the optical depth of the ring. As the optical depth varies with location and time and occulation measurements that coincide with brightness measurements are rarely available, a global "equivalent optical depth" must be computed by minimizing the scatter among multiple measurements. An analysis of both Voyager and Cassini images by French et al. (2014) found that $\tau_{\rm equiv} = 0.035$, consistent with the mean optical depth $\tau = 0.03$ found from analysis of UVIS occultations (Becker, 2016).

In many cases, multiple images of the F ring are taken close in time but at different corotating longitudes. These can be combined into mosaics, and the equivalent widths at different longitudes can be combined to form a longitudinal profile (Figure 1.11). A profile can be averaged to compute the mean ring brightness at a given time or analyzed for the presence of large-scale structure.

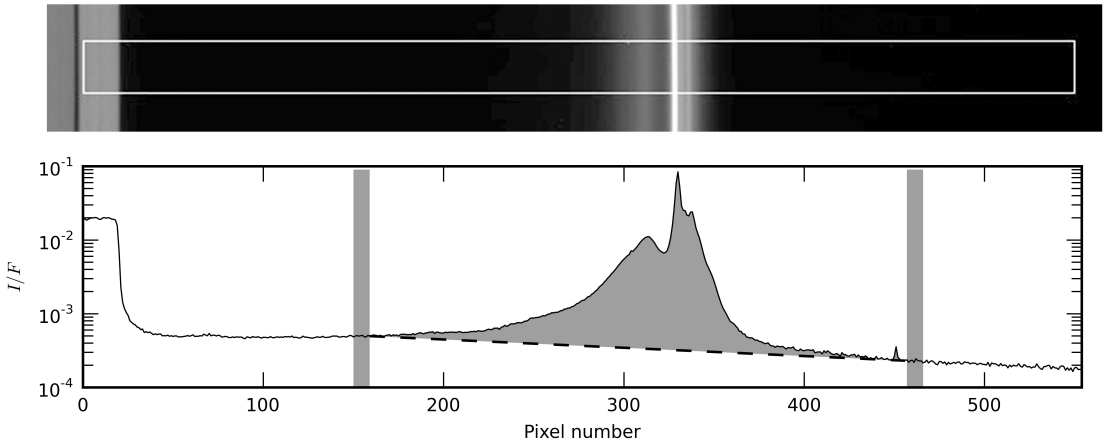

Figure 1.10 Measuring a radial profile from Cassini image N1545556618. A portion of the A ring (and the Keeler gap) is shown on the left and the F ring is on the right. The white box was used to define the dimensions for the radial profile; pixels were averaged in the vertical (longitude) direction to produce the measurements shown. The vertical gray rectangles show the regions used for modeling background contamination and the dashed line shows the background model. The shaded area under the curve shows the region that was integrated to compute the equivalent width. From French et al. (2012).

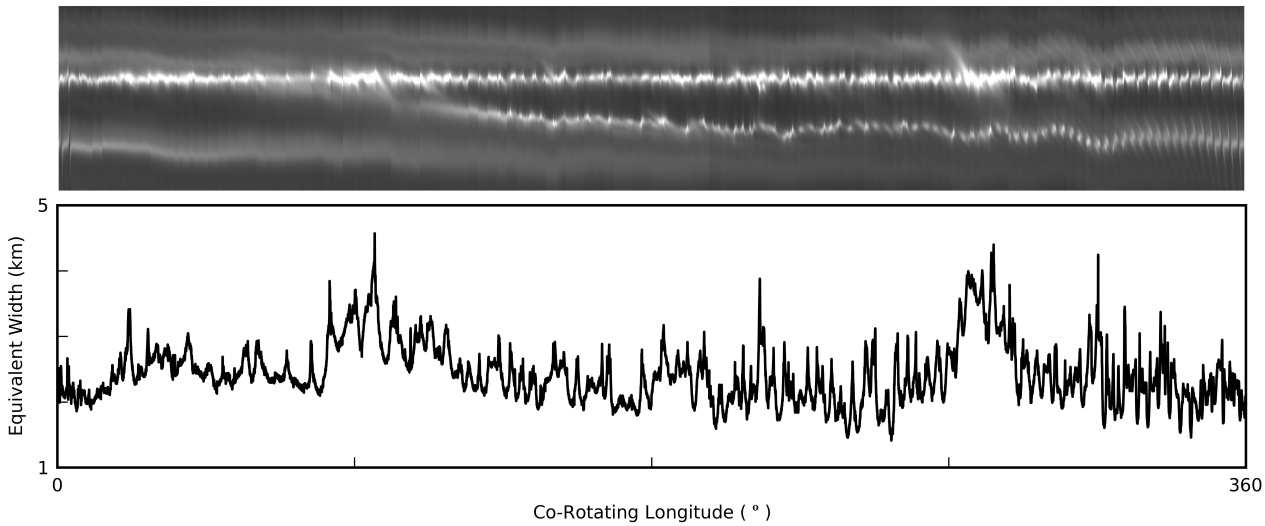

Figure 1.11 The mosaic from Cassini observation ISS_059RF_FMOVIE002_VIMS and its associated equivalent width profile. The radial limits of the mosaic are 139800 (bottom) to 140500 km (top). Note that the radial structure in the image has been discarded in the equivalent width profile, allowing low-resolution observations to be compared on the same footing. From French et al. (2014).

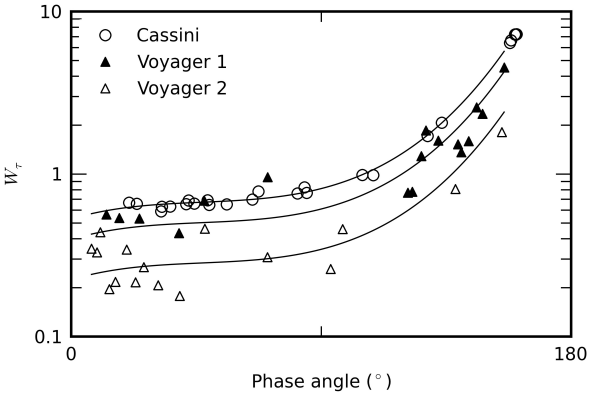

Figure 1.12 F ring phase curve derived from Cassini and Voyager images. Data points give the equivalent width for an entire radial slice of the F ring including the core and skirt region. The top line is the cubic polynomial fit to the Cassini data. This simplified phase curve shape does not attempt to precisely model particle size distribution, but instead is used to roughly compare the brightness of the ring among missions. As the data from Voyager 1 and Voyager 2 have a greater amount of scatter, the curve shape from the Cassini data is also used for the Voyager 1 (middle) and Voyager 2 (bottom) data, assuming the fundamental particle properties governing the phase curve have not changed between missions. From French et al. (2012).

French et al. (2012) performed an analysis of 25 such mosaics as well as 37 measurements taken by Voyager 1 and Voyager 2 (Showalter et al., 1992). To ease comparison of overall brightness, they used a simple cubic polynomial phase curve fit to the more numerous and higher-quality Cassini data, and then assumed that the underlying particle size distribution had not changed between the Cassini measurements and those from the Voyager missions by forcing the Voyager phase curves to have the same shape (but not same average brightness) as the Cassini phase curve. The three phase curves are shown in Figure 1.12. After subtracting a particularly bright anomalous collision event that occurred in late 2006 (see Figure 1.6), they found that the mean ring brightness was 1.3 ± 0.1 times as high during Cassini compared to Voyager 1, and 2.4 ± 0.1 times as high during Cassini compared to Voyager 2.

It is interesting to note that the Cassini data in Figure 1.12 has much less scatter than the Voyager measurements. This scatter is likely the combination of several factors: the ring was actually more variable during Voyager (see Section 1.5), the quality of the Voyager images had a lower signal-to-noise ratio, and the Voyager measurements only sampled a small portion of the ring for each data point (emphasizing local variability) while the Cassini measurements each averaged over a nearly complete ring.

As seen in Figure 1.11 and discussed further in Section 1.5, the F ring shows dramatic azimuthal variation due to the presence of extended bright clumps, while the above analysis used the mean properties of the ring with only a single large and unusual clump removed. As such, it is also interesting to look at the "baseline" ring in the absence of these clumps. Using the equivalent width's 15th percentile as a cutoff and assuming a cubic polynomial fit (French et al., 2014), the F ring phase curve from 50 Cassini profiles is $\log_{10}(P(\alpha)) = a\alpha^3 + b\alpha^2 + c\alpha + d$ with $a = 6.099 \times 10^{-7}$, $b = -8.813 \times 10^{-5}$, $c = 5.517 \times 10^{-3}$, and $d = -0.3296$ with α in degrees. Although the details differ slightly, a similar change in brightness among Voyager 1, Voyager 2, and Cassini was found using this technique, showing that the brightness variation is due mainly to changes in the dimmer skirt rather than the brighter core.

1.4.3 Occultations

Occultations of the F ring, which measure optical depth, are available from a number of sources and at a variety of wavelengths. Optical depth measurements are usually presented as *normal optical depth*, τ, computed by multiplying the observed value by μ. Unlike visible light images, which often provide a view of most or all of the ring, occultations provide information only about a thin radial slice. As occultation observations are usually spread over both time and longitude, each observation must be considered a snapshot of one part of the ring at one instant in time.

There is a simple relationship between optical depth and particle size:

$$\tau(\lambda) = \int_{s_{\min}}^{s_{\max}} Q_{\text{ext}}(s, \lambda) \pi s^2 n(s) ds, \tag{1.5}$$

where Q_{ext} is the extinction efficiency of the particles and $n(s)$ is the differential number density of particles of radius s. For particles much larger than the photon wavelength λ, $Q_{\text{ext}} \to 2$ (Cuzzi, 1985) because the particle diffracts an amount of light equal to the amount it absorbs or reflects. For particles much smaller than λ, $Q_{\text{ext}} \propto s^4$ assuming Rayleigh scattering; these particles do not contribute significantly to the optical depth of the F ring.

Similar to equivalent width, it is convenient to consider the area under the curve of occultation profiles giving *equivalent depth* D (Elliot et al., 1984; French et al., 1991):

$$D = \int \tau(a) da \tag{1.6}$$

The equivalent depth of the F ring has been measured with occultations at various wavelengths over the past three decades. The Voyager 2 PPS instrument observed the passage of the bright ultraviolet star δ Scorpio at 0.264 μm on 1981 Aug 26, yielding an equivalent depth for the core of 0.361 ± 0.044 km and for the envelope of 3.97 ± 0.13 km, giving a total equivalent depth for the ring of 4.33 ± 0.13 km (Showalter et al., 1992). This data was reanalyzed by French et al. (2012) to give a total equivalent depth of 4.57 ± 0.12 km. The PPS occultation data has a low signal-to-noise ratio. Recalibrating this data using information later derived from the Cassini VIMS instrument gives an adjusted equivalent depth of 7.25 km (French et al., 2012).

The Voyager 1 RSS experiment used the Earth-based Deep Space Network to observe the spacecraft's *X*-band (3.6 cm) and *S*-band (13 cm) radio transmission passing through the rings (Tyler et al., 1983; Marouf et al., 1986) (see Figure 1.3). Observations at both wavelengths only revealed

detections of the F ring core, giving equivalent depths of 0.283 ± 0.035 km and 0.153 ± 0.066 km, respectively (Showalter et al., 1992).

Cassini VIMS observed the occultation of a variety of stars by the F ring at 2.92 μm between 2005 and 2009. An aggregation of 30 of these measurements yields an equivalent depth of 9.99 ± 2.65 km (French et al., 2012). Likewise, Cassini UVIS observed various occultations at $110 - 190$ nm between 2005 and 2008. Analysis of 93 observations yields equivalent depths for the F ring ranging from 3.9 to 50.8 km, with a median of 9.7 km (Albers et al., 2012).

Finally, Poulet et al. (2000a) and Bosh et al. (2002) used HST observations to derive equivalent depths at a variety of wavelengths. A summary of all equivalent depth findings is given in Table 1.2.

1.4.4 Particle size distribution

The F ring consists of both a narrow core that is the dominant feature in occultations but is not optically resolved and a dusty skirt that contributes the majority of the scattered light. A variety of techniques have been used to place limits on particle size and distribution. The particle size distribution of rings is often characterized by a simple power law:

$$n(s) = n(s_0)\left(\frac{s}{s_0}\right)^{-q}, \tag{1.7}$$

where s_0 is a reference particle size. A large q implies that a relatively larger number of small particles dominates the scattering.

The first analysis of the particle size distribution of the F ring was conducted by Tyler et al. (1983) and Marouf et al. (1986), who examined occultation data from the Voyager RSS experiment. They found that, with careful processing, the F ring core could be detected at 13 cm, implying a population of particles at least that large. Analysis of joint RSS observations determined that roughly 40% of the opacity of the core is due to particles with radii exceeding ~ 4 cm.

Showalter et al. (1992) performed the only analysis of the F ring phase curve to date that attempted to derive the particle size distribution. They assumed the F ring had two fundamental particle populations: "small" particles, with dimensions comparable to the wavelength of light that can be described by a variant of Mie theory (in this case the randomly-oriented, nonspherical models from Pollack and Cuzzi (1980)), and "large" particles, which are strongly influenced by macroscopic surface properties and are modeled using the high-albedo icy moon Europa as an analog. The small-particle population was assumed to obey a power law with slope q. In addition, they modeled a free parameter f, the fraction that "small" particles contribute to the overall optical depth. As only poorly-resolved Voyager images were available, the analysis did not attempt to distinguish between the core and skirt regions, although it is reasonable to assume that the core contains the majority of the large particles. Their best fit model (Figure 1.13) corresponds to $q = 4.6 \pm 0.5$ and $f = 1.00^{+0.00}_{-0.02}$. These results apply to particle sizes in the approximate range $0.03 - 1\mu$m. Such a large dust fraction is consistent with $f > 0.80$ determined

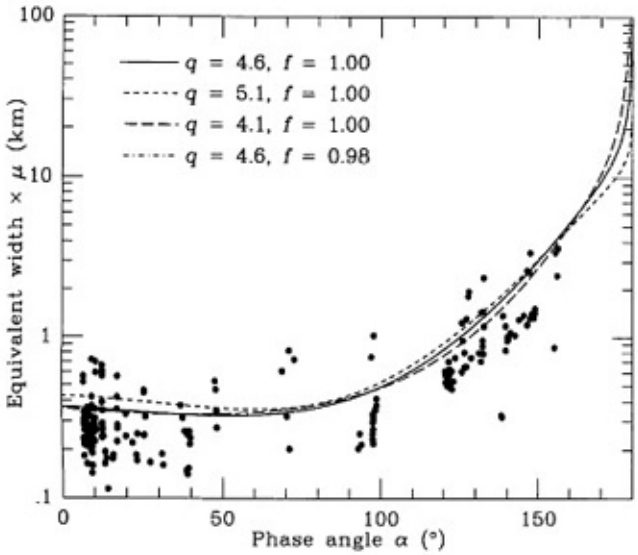

Figure 1.13 Normal equivalent width measurements from Voyager 1 and 2 observations and best-fit phase curves. q is the power law exponent of the small particles, where the number of particles of size a is $n(s) \propto s^{-q}$, and f is the fraction that the small particles contribute to the overall optical depth. Unlike the simplified phase curves in Figure 1.12, the phase curves here attempt to capture the actual characteristics (size distribution and shape) of the ring particles. From Showalter et al. (1992).

by Poulet et al. (2000a) from HST observations of the 1995 Saturn ring plane crossing.

Such a steep slope is surprising; in comparison, the size distribution of collisional ejecta is $q = 3.4$ (Grun et al., 1984). The steep slope of the skirt (assumed to consist primarily of "small" particles) is far steeper than for the dust at Jupiter ($q = 2.5 \pm 0.5$ (Showalter et al., 1987)) or Uranus ($q = 2.5 \pm 0.5$ (Ockert et al., 1987)). As drag forces (such as Poynting-Robertson and plasma drag) tend to flatten a size distribution (Burns et al., 1984), this implies that drag forces may not play a major role in the F ring. However, a more plausible explanation may be that the brightness of the F ring changed dramatically between Voyager 1 and 2. As can be seen in Figure 1.12, the measurements from Voyager 1 appear to be much brighter than those from Voyager 2. At the same time, the data from Voyager 1 are heavily weighted towards the high phase angles while those from Voyager 2 are more weighted towards the low phase angles. Showalter et al. (1992) combined data from both spacecraft before fitting the phase curve and, as the best-fit model is extremely sensitive to the phase curve shape, the result may have been affected by the merging of these sets of data. French et al. (2012) also note the increase in brightness of the F ring with increasing phase angle, suggestive of a higher percentage of small, forward-scattering particles that have persisted in the region for over 30 years. Thus, although it is clear that the ring skirt is dominated by dust, the steep power law slope found by Showalter et al. (1992) may not be accurate.

Showalter et al. (1992) also analyzed the Voyager occultation observations of the F ring core (Table 1.2). If we assume

Table 1.2. *Summary of equivalent depths of the F ring in order of increasing wavelength.* [1]*Albers et al. (2012).* [2]*Showalter et al. (1992).* [3]*French et al. (2012).* [4]*Poulet et al. (2000a).* [5]*Bosh et al. (2002).* [†]*PPS value has been adjusted based on VIMS data to simulate having a higher signal-to-noise ratio.* [‡]*Mean and standard deviation of 30 VIMS measurements. Disagreement among analyses of Voyager 2 PPS data is due to differing assumed widths of the F ring core: Albers et al. (2012) assumed the core is 50 km wide (approximately the width of the entire ring assumed by Showalter et al. (1992)) while Showalter et al. (1992) assumed the core is 1 km wide.*

Date	Object	Instrument	Wavelength	Core (km)	Envelope (km)	Total (km)
2005 – 2008	Various	Cassini UVIS[1]	110 – 190 nm	4.7 (2.4 – 6.9)		9.7 (3.9 – 50.8)
1981 Aug 26	δ Sco	Voyager 2 PPS[2]	264 nm	0.361 ± 0.044	3.97 ± 0.13	4.33 ± 0.13
1981 Aug 26	δ Sco	Voyager 2 PPS[3]	264 nm			4.57 ± 0.12
1981 Aug 26	δ Sco	Voyager 2 PPS[3†]	264 nm			7.25
1981 Aug 26	δ Sco	Voyager 2 PPS[1]	264 nm	4.1		
1981 Aug 26	δ Sco	Derived from PPS[2]	500 nm			5.0 ± 0.3
1995 Nov 21	GSC5249-01240	HST FOS[5]	270 – 740 nm			7.41 ± 0.15 km
1995 Aug 10	Reflected light	HST WFPC2[4]	890 nm			8 ± 3
1989 Jul 03	28 Sgr	McDonald (ingress)[5]	2.1 μm			2.8 ± 0.1
1989 Jul 03	28 Sgr	McDonald (egress)[5]	2.1 μm			3.6 ± 0.1
1995 Nov 21	GSC5249-01240	IRTF[5]	2.3 μm			5.76 ± 0.06
2005 – 2009	Various	Cassini VIMS[3‡]	2.92 μm			9.99 ± 2.65
1989 Jul 03	28 Sgr	IRTF (egress)[5]	3.1 μm			3.79 ± 0.08
1989 Jul 03	28 Sgr	Palomar (ingress)[5]	3.9 μm			3.0 ± 0.1
1980 Nov 13	Voyager 1 RSS *X*-band	DSS-63[2]	3.6 cm	0.283 ± 0.035		0.283 ± 0.035
1980 Nov 13	Voyager 1 RSS *S*-band	DSS-63[2]	13 cm	0.153 ± 0.066		0.153 ± 0.066

that a power-law size distribution applies in the core as well, the X-band/S-band equivalent depth ratio provides a direct measure of the power law slope, $q = 3.5 \pm 0.4$ (valid over the size range 0.01 cm to 10 m), consistent with that of collisional ejecta. Assuming the core is what is seen in the narrowest peak of the PPS occultation, the PPS core/X-band optical depth ratio gives a lower size cutoff of $r \sim 0.1$ cm.

Bosh et al. (2002) observed the occultation of GSC5249-01240 by Saturn's rings with the Faint Object Spectrograph on the HST. They found that the F ring's equivalent depth was constant between 0.27 and 0.74 μm, indicating the presence of ring particles larger than ~ 10 μm. They further determined that the particle size distribution has a slope $q \sim 3$ with 10 μm $< a_{\max} <$ 2 m.

In contrast, occultation measurements of the F ring by the Cassini VIMS instrument in the range $0.85 - 5.0$ μm do show a noticeable reduction in the optical depth in the vicinity of 2.87 μm (Hedman et al., 2011; Vahidinia et al., 2011). The dip in optical depth is likely caused by the Christiansen Effect (Christiansen, 1884, 1885), a reduction in the extinction of small particles when their real refractive index is close to that of the surrounding medium while their complex refractive index is much less than unity. A Christiansen wavelength of 2.87 μm corresponds to crystalline water ice. In addition, the strength of this dip is highly sensitive to the particle size distribution.

Hedman et al. (2011) found that a broken power law was required to reproduce the observed transmission spectral features. This model consists of one power law $n(s) \propto s^{-q_{\rm small}}$ for particles below a size $s_{\rm break}$ and another power law $n(s) \propto s^{-q_{\rm big}}$ above that size. Due to differences in assumed $s_{\rm break}$ and the unknown regolith characteristics of the ring particles, it is not possible to produce a unique set of power law slopes using only transmission spectra. However, assuming $s_{\rm break} \sim 10$ μm, $q_{\rm small} \sim 2$ and $q_{\rm big} \sim 3.5$ is necessary to reproduce the basic spectral features (Figure 1.14). The lack of a spike in optical depth at $\lambda \sim 3.1$ μm suggests that the ring, in general, is depleted of sub-micron-sized particles. In addition, the dip in extinction spectra tends to be stronger in regions with lower optical depth; larger particles appear to be more concentrated in denser parts of the ring.

As always, the variability of the F ring makes analysis difficult, and a spread of spectral features is observed across the occultations. However, certain features stand out as unique; one such is shown in Figure 1.15. While the majority of the ring commonly shows a different optical depth at $\lambda \sim 2.9$ and $\lambda \sim 3.2$ μm, the sharp peak is approximately the same at the two wavelengths. This implies that the region measured at the peak contains a much smaller fraction of micron-sized particles than the rest of the F ring, and may represent the detection of a small clump of debris. Hedman et al. (2011) detected 14 such spectral features with diverse morphologies. Such clumps may be the progenitors of more solid clumps embedded in the core, as detected by UVIS occultations (Esposito et al., 2008; Meinke et al., 2012) and Cassini imaging (Murray et al., 2008; Beurle et al., 2010) (see Section 1.7).

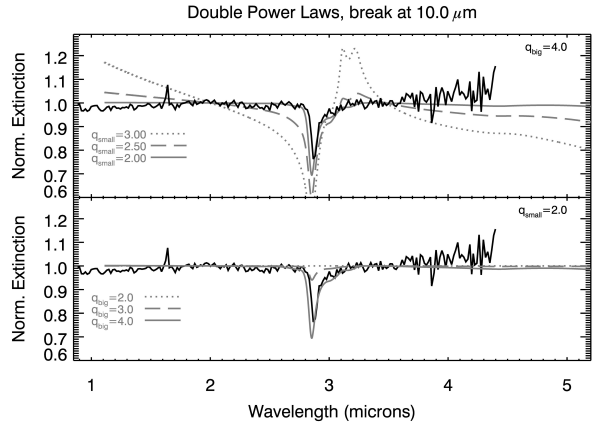

Figure 1.14 Model extinction spectra for various particle size distributions using a broken power law with $s_{\rm break} \sim 10$ μm (grey) compared with the observed spectra derived from the Rev 46 α Orionis occultation (black). (Top) $q = 4.0$ above the break and as indicated below the break. (Bottom) $q = 2.0$ below the break and as indicated above the break. From Hedman et al. (2011).

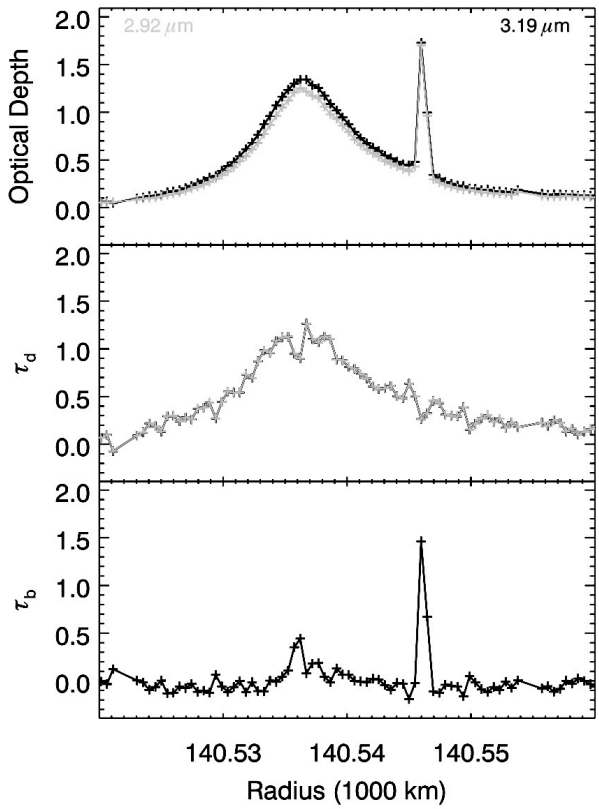

Figure 1.15 (Top) Optical depth profiles from the Rev 013 egress α Sco occultation at 2.92 μm and 3.19 μm. (Middle) The inferred optical depth in dust. (Bottom) The inferred optical depth in excess large particles. From Hedman et al. (2011).

Vahidinia et al. (2011) analyzed high-phase-angle VIMS transmission spectra with a model based on Mie scattering combined with Effective Medium Theory and constrained the range of particle sizes in the F ring skirt to $10 - 30$ μm. However, this model, based on porous spherical ice particles, failed to precisely match the 2.87 μm Christiansen feature. A more advanced model using a Discrete Dipole Approximation showed that the $10 - 30$ μm particles can be successfully modeled as aggregates composed of individual monomers ranging in radius from $1 - 3$ μm.

Finally, Becker (2016) analyzed 13 UVIS Extreme Ultraviolet occultations of the Sun by the F ring. Depending on the exact portion of the occultation being observed, these measurements can combine the reduction in photon count due to the occultation with the increase in photon count due to diffraction by small ring particles. Such signal enhancements are difficult to detect, however, because the projected diameter of the Sun on the F ring is much larger than the width of the ring's core. As a result, not all occultations contained signal enhancements of the unocculted sunlight outside of the F ring, which would indicate diffraction by relatively small particles. Those that did likely indicated a larger quality of small particles present at the occultation site. In some cases, the occultations could be compared with Cassini ISS images taken at the same longitude at approximately the same time. Those occultations that showed signal enhancements due to diffraction correlated well with images that showed collisional features, while occultations not containing signal enhancements correlated with images that showed a more quiescent ring. Modeling showed that in the area near collisional features, ring particles had a minimum radius of < 10 μm and $q \sim 2.8 - 3.5$, while in the quiescent areas ring particles had minimum radii ≥ 100 μm. In all cases the mean optical depth was $\tau \sim 0.03$. This contrasts with Vahidinia et al. (2011), who found that the ~ 10 μm particles were visible regardless of longitude. Further analysis will be required to reconcile these two results.

In summary, although results differ to some extent, the F ring clearly consists of particles tens of microns in diameter and larger, with smaller particles present further from the core and possibly also in areas of collisional activity.

1.4.5 Radial Width

The width of the F ring is a difficult measurement to define, as the ring does not have sharp edges; rather, the ring material simply gets more diffuse the further you get from the core. French et al. (2012) defined the photometric width as being the radial extent that encompasses 90% of the total equivalent width. Using Cassini ISS images from $2004 - 2009$ they found a mean width of 580 ± 70 km. This result is consistent with the width of ~ 500 km that Becker (2016) found was necessary to properly model UVIS occultation behavior. A similar analysis of 59 Voyager 1 ISS images (French et al., 2012) yielded a mean width of 200 ± 40 km, showing that the ring during the Cassini era was nearly three times as wide as during Voyager. It is tempting to blame the lower signal-to-noise ratio of the Voyager images for this difference, but a reprocessing of the Cassini images by French et al. (2012)

to downgrade them to the quality of the Voyager images resulted in a change in width of at most 10%.

French et al. (2012) also found that in the Cassini images there was a slight dependence of width on phase angle, with greater widths generally detected at higher phase angles; although data were limited, a similar trend was visible in the Voyager 1 images. This reinforces the above conclusion that smaller particles are found further from the core; they become more visible at higher phase angles. French et al. (2012) also applied their definition of radial width to 30 VIMS occultations, finding a mean width of 370 ± 60 km. This width is smaller than the radial width found using visible-light images, suggesting that the core is sufficiently dense that not all particles can be seen in reflected sunlight, consistent with the earlier observation that shadowing and obscuration are necessary to fully model the F ring's photometric properties.

1.5 Extended Clumps

In addition to the small ($\ll 1^\circ$ longitude), embedded clumps, the F ring shows variation on large ($3-40^\circ$) scales as well (Figure 1.16). These *extended clumps* (ECs) have been seen by Voyager 1 and 2 (Showalter, 2004), Cassini (French et al., 2014), and the Hubble Space Telescope during the 1995 ring plane crossing (McGhee et al., 2001; Bosh and Rivkin, 1996). The number, orbital position, lifetime, angular width, and brightness of the ECs has remained fairly constant over this time period. On average, there are $2-3$ major and $20-40$ minor ECs present at any given time. They have semi-major axes that are normally distributed ~ 40 km on either side of the F ring core (Figure 1.17). Angular widths are concentrated around $5-10^\circ$ in longitudinal extent, with a long tail at larger sizes (Figure 1.18).

The exact lifetime of ECs is difficult to determine due to the nature of the available observations. The tightest constraints show that some ECs could not have lasted for more than ~ 25 days while others last for at least ~ 3 months. However, no ECs survived the 9-month gap between Voyager missions or were observed for more than ~ 6 months during the 1995 Earth-ring plane crossing (McGhee et al., 2001; Bosh and Rivkin, 1996). The origin of these ECs remains a mystery, as the lack of continuous observation has prevented detailed observations of their initial formation. However, French et al. (2014) were able to constrain the creation timescale of one EC through a series of FMOVIEs (Figure 1.19). In this case, the EC appears to grow from an otherwise dormant region of the ring with no obvious cause. Attempts to link the creation of ECs to the location of Prometheus have failed.

The eventual disappearance of ECs is similarly shrouded in mystery. While one would expect the ECs (which have non-zero radial extent) to spread through Keplerian shear and eventually become sufficiently stretched that they fade into the background ring material, observations instead show that ECs disappear much more rapidly than can be explained solely from Keplerian shear (Figure 1.20).

The number of extremely bright ECs is quite different between the Voyager and Cassini observations. While such ECs were common during the Voyager era, with several being visible at any one time, only two such bright ECs were seen during the entire six years of Cassini observations analyzed by French et al. (2014). With the benefit of the high-resolution images available from Cassini, French et al. (2014) found that the two bright ECs corresponded to obvious impact events, where the impacting body was visible both before and after the collisions (Murray et al., 2008). If the bright ECs seen during Voyager had a similar cause, this would suggest that the number of impact events has dramatically decreased during the intervening 30 years. Such a decrease could be explained by a reduction in the population of impactors or a decrease in their relative velocity with the F ring core.

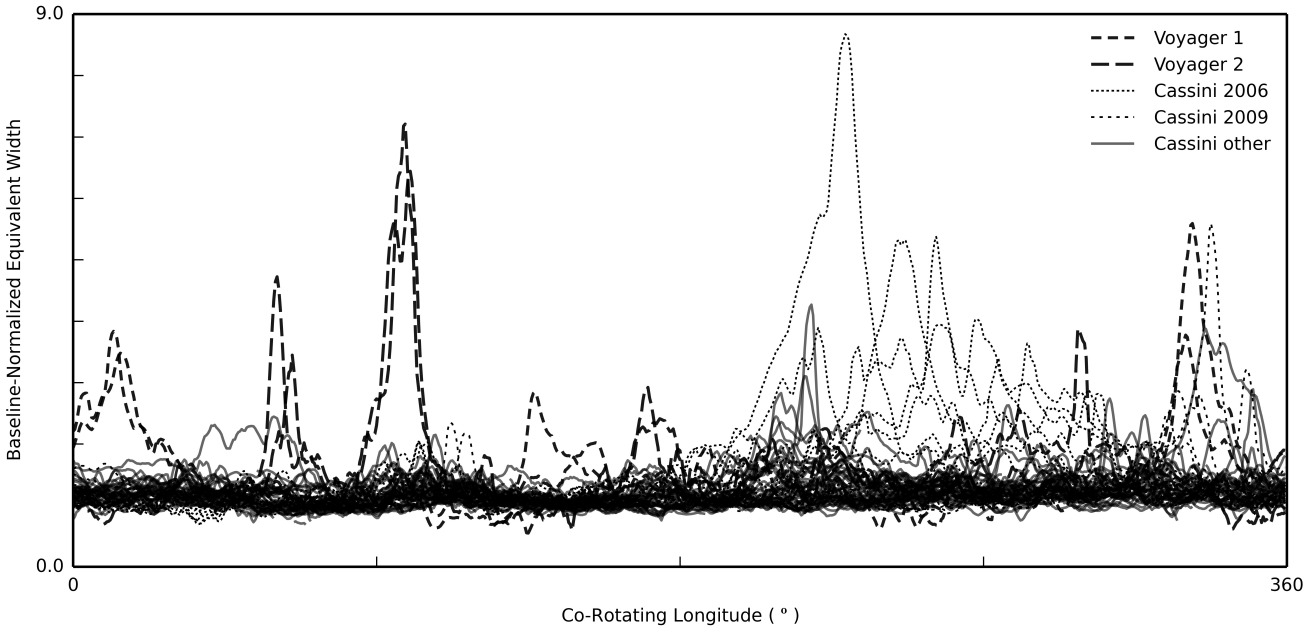

Figure 1.16 Longitudinal profiles from Voyager and Cassini. All profiles have been normalized to the 15th percentile value, which represents the non-clump brightness of the ring. The Cassini 2006 and Cassini 2009 curves represent data from those years; during each of these time periods an anomalous bright extended clump formed and dissipated. With the exception of those two years, the Voyager data clearly contained more and brighter extended clumps than the Cassini data did. From French et al. (2014).

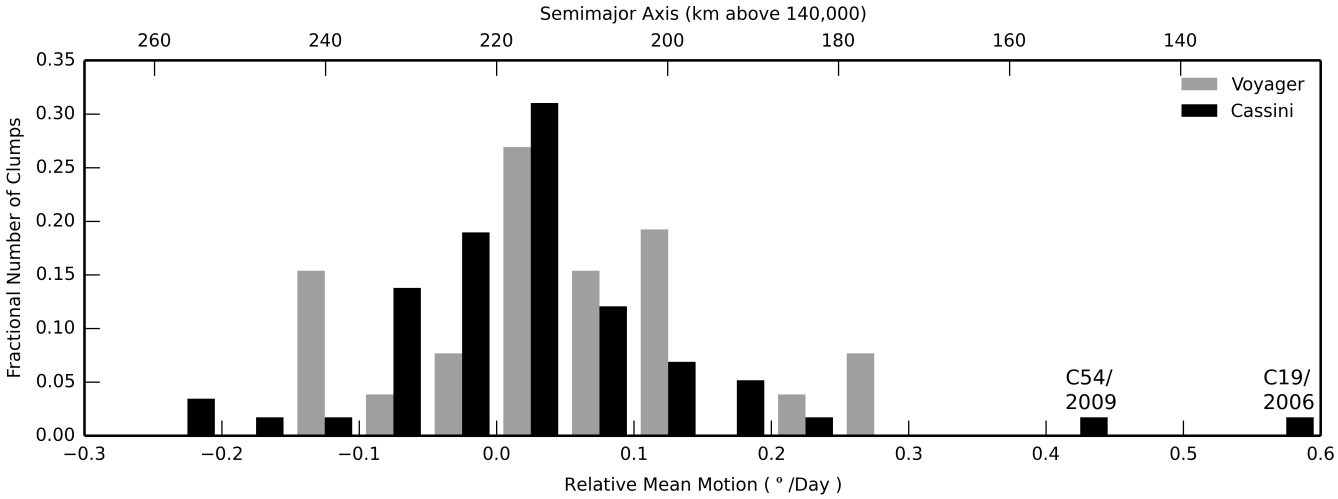

Figure 1.17 Distribution of semi-major axes for Voyager and Cassini ECs. The ECs are generally centered on the F ring core but can be found within 40 km on either side. C54/2009 and C19/2006 are anomalous bright clumps likely the result of major collisions with the F ring core (see Figures 1.16 and 1.6). Note that this figure, which covers extended clumps, differs from Figure 1.8, which covers very small localized clumps. However, in both cases the features are found close to the core. From French et al. (2014).

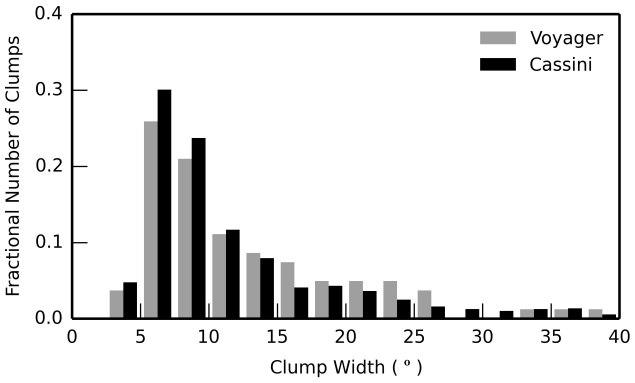

Figure 1.18 Distribution of angular widths for ECs from Voyager and Cassini observations. The cut-off at the low end is artificial because any ECs with angular widths less than 3° are ignored. There is no significant difference between the two time periods. From French et al. (2014).

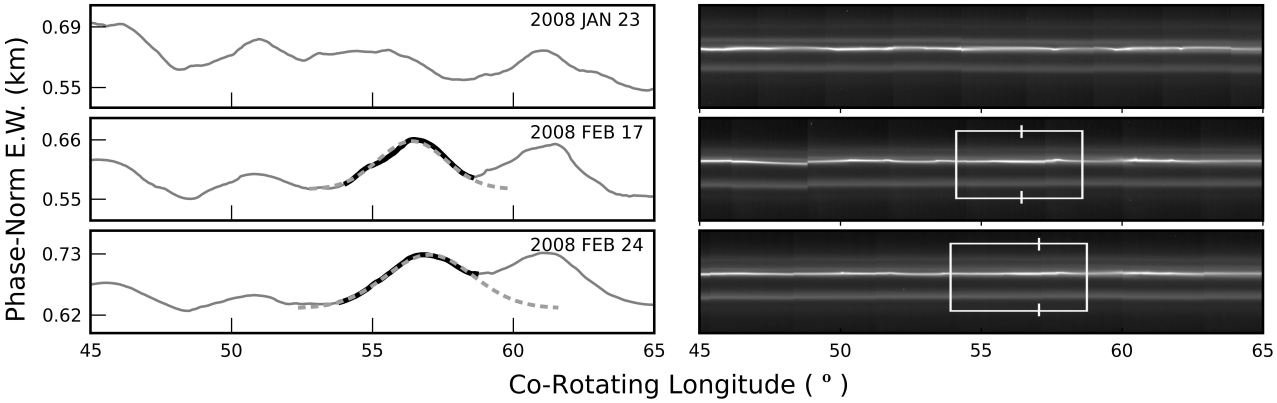

Figure 1.19 The formation of an extended clump over approximately one month. The left plots show longitudinal profiles of equivalent width for three different dates; the solid lines show a 20° excerpt of the complete profile and the dashed lines show Gaussian fits to the extended clump. The right images show excerpts from contrast-stretched mosaics covering the same longitudes; the white boxes indicate the longitudinal extent of the ECs as determined by the Gaussian fit. The EC appears to arise from an otherwise dormant region of the ring. From French et al. (2014).

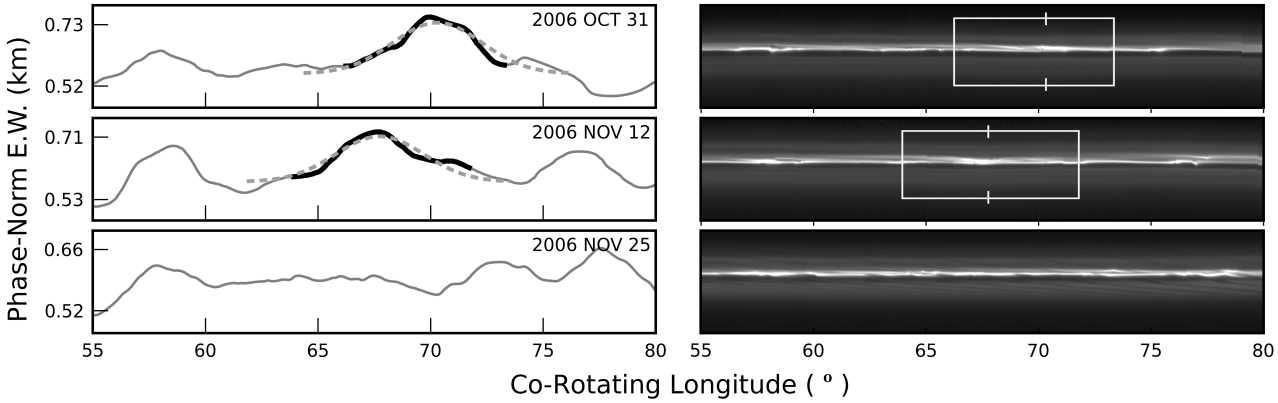

Figure 1.20 The disappearance of an extended clump over approximately one month. The left plots show longitudinal profiles of equivalent width for three different dates; the solid lines show a 25° excerpt of the complete profile and the dashed lines show Gaussian fits to the extended clump. The right images show excerpts from contrast-stretched mosaics covering the same longitudes; the white boxes indicate the longitudinal extent of the ECs as determined by the Gaussian fit. The EC appears to disappear into the background ring material without being sufficiently stretched by Keplerian shear. The EC moves in co-rotating longitude over time because it has a semi-major axis slightly different from that of the F ring core. From French et al. (2014).

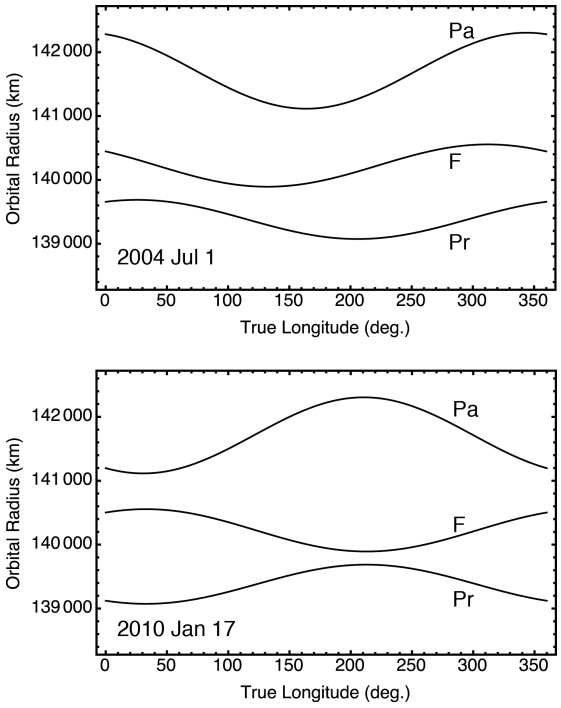

Figure 1.21 The relative orbits of Prometheus (Pr), Pandora (Pa) and the F ring (F) on 2004 July 1, the start of the Cassini orbital tour, and on 2010 January 17, when Prometheus had its closest approach to the F ring. From Murray et al. (2017).

1.6 The effect of Prometheus

With two satellites orbiting on either side of the F ring, it is natural to assume that they would be the main perturbers of the ring. Although Pandora does have a measurable effect on the ring, Prometheus is 16% more massive and has a separation in semi-major axis from the ring that is approximately half that of Pandora (Cooper et al., 2015). However, the size of the perturbation is time-variable because the orbits of the ring and both satellites are eccentric and subject to different apsidal precession rates due to Saturn's oblateness. The effect of this on the orbital configurations is illustrated in Figure 1.21, where we show the relative orbits of all three objects in the system in July 2004, at the start of Cassini's orbital tour, and in January 2010, when the orbits of Prometheus and the F ring had their minimum separation. The plots were derived using the orbits of Prometheus and Pandora from Jacobson et al. (2008) and the orbit of the F ring from Cooper et al. (2013) (see Table 1.1 above). The calculated separation of Prometheus and the F ring was 460 km in 2004 but had reduced to 206 km by 2010. The changing separation is dominated by the differences in precession rates and has a period of $\sim$ 19 years. Therefore we would expect the nature of the phenomena Prometheus induces in the F ring to vary on that timescale.

The Voyager cameras did not capture images of Prometheus' interaction with the F ring. Indeed, the best evidence for the type of structures that could be created was first seen in numerical simulations (see, e.g. (Showalter and Burns, 1982; Kolvoord and Burns, 1992; Giuliatti Winter, 1994; Murray, 1994)). These results showed that the varying distance between Prometheus and the ring over one orbital period caused the appearance of the perturbed ring to vary on the same timescale. If we let n and a be the mean motion and semi-major axis respectively of a ring particle and let $n_{\rm s} = n + \Delta n$ and $a_{\rm s} = a + \Delta a$ be the mean motion and semi-major axis of an adjacent satellite (e.g. Prometheus) then the number of orbits between conjunctions of the two is $|n/\Delta n|$. In that number of orbits the ring particle will have traveled a distance $2\pi\, a$ with respect to the satellite. From Kepler's Third Law, $\Delta n = -(3/2)(\Delta a/a)n$. Hence we would expect to see structure in the ring with a wavelength

$$\lambda = \frac{2\pi\, a}{|n/\Delta n|} = 3\pi|\Delta a|\,. \tag{1.8}$$

In terms of degrees of longitude on the ring the wavelength

$$\Lambda = 360^\circ \frac{\lambda}{2\pi\, a} = 540^\circ \frac{|\Delta a|}{a}\,. \tag{1.9}$$

Therefore, using the semi-major axis data from Jacobson et al. (2008) and Cooper et al. (2013), we would expect Prometheus to produce features at intervals of 3.25° at the F ring's core with shorter wavelengths closer to the satellite. This is consistent with what is seen in Figure 1.4c,d, Figure 1.6 (between corotating longitudes of 200° and 260°) and Figure 1.11 (between corotating longitudes 300° and 360°). Note that the wavelength is independent of the mass of the satellite. Figure 1.22 shows a reprojected 45° segment of the F ring derived from Cassini NAC images obtained in April 2005. The regular pattern caused by Prometheus is obvious across the whole region just encountered by the satellite.

Murray et al. (2005) examined the nature of the perturbations created by Prometheus and their effect on the ring. They carried out numerical simulations of Prometheus' interaction with the F ring and showed how the time variations of the ring's appearance in Cassini images matched those seen in the simulations. Once conjunction has taken place and the resulting, near-instantaneous perturbation has occurred, the ring particles proceed on their perturbed paths experiencing no further perturbations – collisional processes and self-gravity were not included. As the cycle repeats itself with the next conjunction so too does the pattern imprinted on the ring by the satellite. Murray et al. (2005) named the resulting, time-varying pattern the "streamer-channel" phenomenon after the two extremes of structures that result: (i) when Prometheus is near its periapse and therefore furthest from the ring there is a concentration of ring material (a "streamer") connecting the satellite to the ring but (ii) when Prometheus is at its apoapse and closest to the ring "channels" in the ring material are apparent. The cycle of alternating between streamers and channels is repeated downstream of Prometheus. However, although we can consider that the initial structures are imprinted almost radially over a range of semi-major axes, Keplerian shear is also present. This accounts for the changing slope of features with longitude seen in both the simulations and the Cassini images.

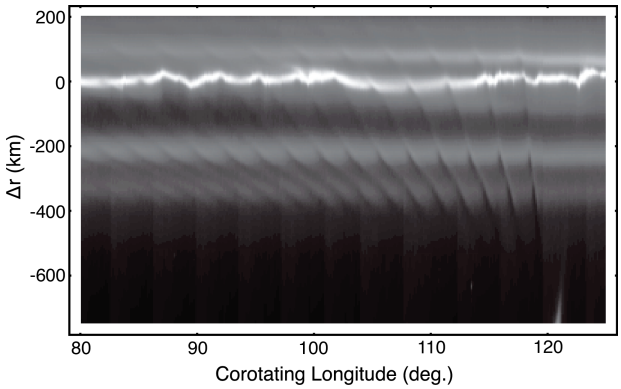

Figure 1.22 A mosaic of enhanced, reprojected images of the F ring region derived from an FMOVIE sequence taken on 2005 April 13. Prometheus is just below the field of view close to a corotating longitude of 121°. The sequence of dark bands, (the "channel" phase of the "streamer-channel" phenomenon) apparently emanating from Prometheus but trailing it, are caused by perturbations from the satellite. At the F ring core ($\Delta r \approx 0$) the separation in longitude is close to the predicted wavelength of $\Lambda = 3.25°$.

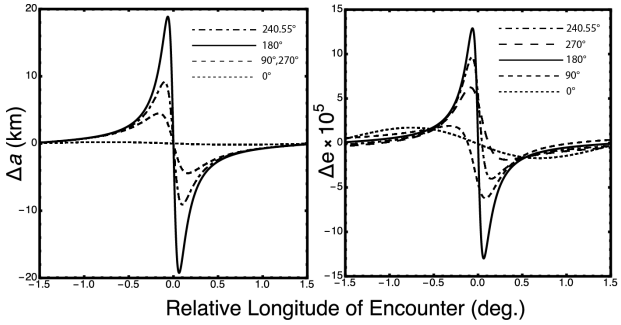

Figure 1.23 The measured changes in semi-major axis (left; cf. Figure 4 of Beurle et al. (2010)) and eccentricity (right) as a function of the relative longitude of encounter for test particles in the F ring having conjunctions with Prometheus. The different curves show the results for different offsets in periapse between Prometheus and the F ring core. The offset of 240.55° corresponds to the periapse difference at the epoch of 2007 January 1 12:00. The data is taken from the results described by Williams (2009).

The dynamics of the streamer-channel phenomenon were studied in some detail by Williams (2009). Murray et al. (2017) used data from Williams (2009) to show how the expected changes in orbital elements can explain the subsequent structure seen in the ring. Figure 1.23 shows plots of the measured changes in semi-major axis and eccentricity derived from numerical integrations for different relative orientations of the orbits of Prometheus and the F ring. Note that the changes in these elements are highly correlated and that the maximum (positive and negative) changes do not occur at zero relative longitude but rather just to either side of it. We can use the data in these plots to help visualize the streamer-channel process.

The motion of objects on Keplerian elliptical orbits of semi-major axis a and eccentricity e can be visualized as epicyclic motion around a centered ellipse, the center of which is moving at a constant rate equal to the mean motion around the central body. The centered ellipse has axes of length $2ae$ and $4ae$, i.e. in the ratio 2 : 1 (see, e.g., the section on epicyclic motion in Murray and Dermott (1999)). Figure 1.24 shows the results of modeling the creation and evolution of 51 particle orbits perturbed by an encounter with Prometheus at its apoapse when its orbit is anti-aligned with that of the F ring (i.e. with a periapse difference of 180°). At time $t = 0$ each particle is assigned its perturbed ellipse based on the values shown in Figure 1.23; particles with negative encounter longitude will be at their periapse and those with positive encounter longitude will be at their apoapse. The system is then evolved in its predetermined manner. The effects of Keplerian shear are taken into account by shifting the center of each epicycle to the left or right by the appropriate amount according to whether it has $\Delta a > 0$ or $\Delta a < 0$, respectively. Note that the single particle at the origin does not receive any perturbation, in accordance with theory and the numerical results shown in Figure 1.23.

The evolution of the particles shown in Figure 1.24 explains several features seen in both the simulations and the images of the rings. Note that at integer multiples of orbital periods (i.e. $t = 0, 4, 12$) the particles all return to their approximate initial orbital phases (i.e. periapse or apoapse) at which times the ring would give the appearance of being unperturbed, albeit with an ever-widening gap at the location where the original Prometheus perturbation took place. This would correspond to the "channel" phase of the "streamer-channel" cycle. In contrast, at half-integer values of the orbital period (e.g. $t = 3.5, 11.5$) the approximate orbital phases of the particles differ from their initial values by 180° and the ring appears to be at its most distorted with ring particles taking up position along a diagonal line (of ever decreasing slope) across the gap. Of course, in reality the only perturbation was the initial one caused by the impulsive encounter with Prometheus. The ring's appearance at the half-integer values of the orbital period would be consistent with it being at the streamer phase of the "streamer-channel" cycle. The shearing of the particle orbits and their distortion is always most evident at the half-integer values of the orbital periods. In fact, the resulting streamer at this orbital phase is always aligned in the direction of Prometheus' orbital location off to the lower right.

At time $t = 3.5$ orbital periods the particles which were at periapse are now at apoapse and vice versa, and the ellipses have also shifted due to Keplerian shear. It can be seen that the particles on orbits with the largest Δa have evolved the most rapidly, to the extent that there is an accumulation of ellipses at $\pm 0.3^\circ$. In images this would correspond to a brightening of the rings at the edge of the channels and this is indeed what is observed. Beyond this time the movement of particles around their shifted epicycles means that as the particles move towards the line of zero relative radius, the surface density of particles will increase leading to the production of clumps. This continues to occur until the largest epicycles have passed through the smallest. This has mostly occurred by the last two frames, $t = 11.5, 12$ orbital periods. Therefore the observed distortions in the ring can now be explained simply on the basis of perturbed particles moving along their pre-determined epicycles.

Another feature of the F ring that can be explained by this model is the widening of the gaps and the appearance of a residual ring at the orbital phase where channels are evident. If we ignore the particles initially between encounter longitudes of $\pm 0.05^\circ$, then in each cycle the gap is most visible when the particles return to the initial orbital phase, i.e. at periapse to the left and at apoapse to the right ($t = 4, 12$ orbital periods in Figure 1.24). This occurs when Prometheus is at the apoapse of its orbit, even though it is no longer in the vicinity of this 1° section of ring. However, at such times the small number of particles with initial encounter longitudes in the range $\pm 0.05^\circ$ are still located in what has become the gap. This is neatly illustrated in Figure 1.25, which is a Cassini NAC image of the F ring with one bright inner strand. Inspection of the most recent channel (left of center) shows a line of material across the inner strand as well as a narrowing at the orbit of the core. We also note a wedge of material in the same channel, inwards of the in-

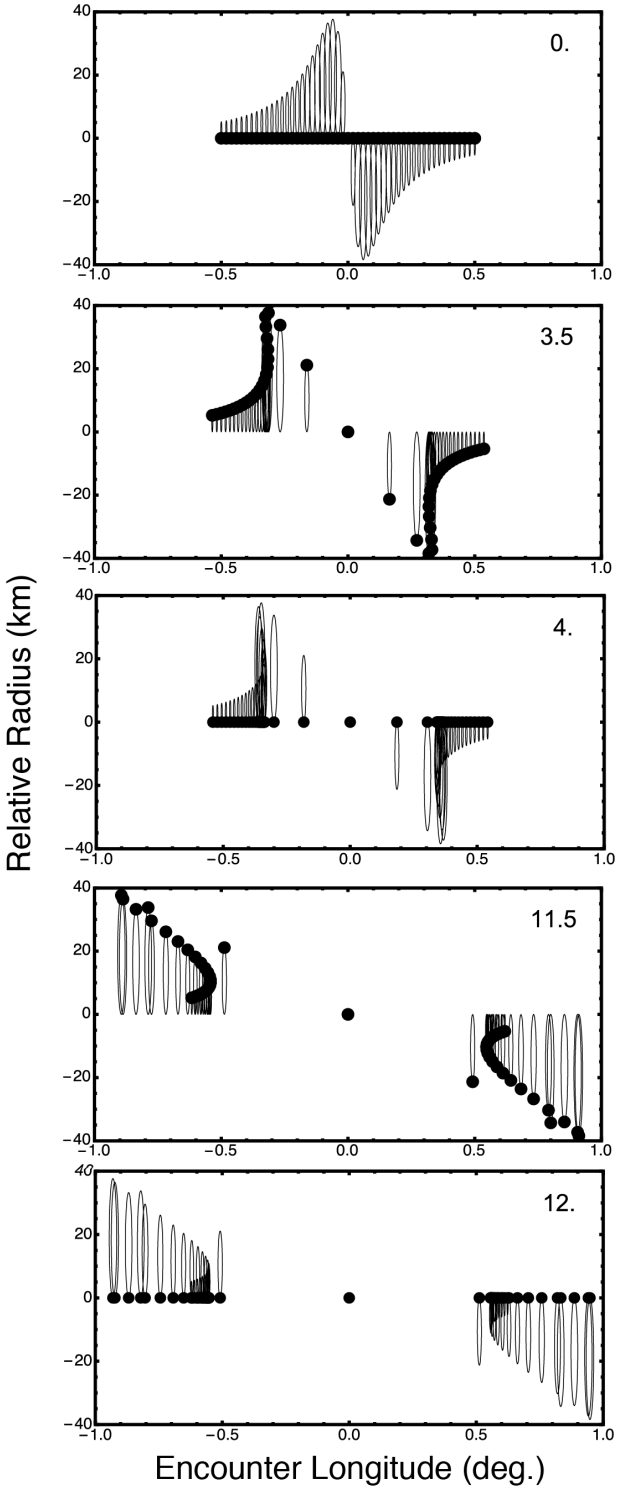

Figure 1.24 The time evolution of 51 test particles assigned a perturbed semi-major axis, Δa, and a perturbed eccentricity, Δe, based on the data shown in Figure 1.23. The time in orbital periods is shown at the top right of each frame. Each particle moves clockwise around a centered ellipse of length $4\Delta a\,\Delta e$ and height $2\Delta a\,\Delta e$. The perturbation is applied at time $t = 0$ and the relative positions are shown at non-equal intervals up to a maximum time of 12 orbital periods later. See main text for additional information. Adapted from Murray et al. (2017). An animation of the entire sequence is available as an online movie.

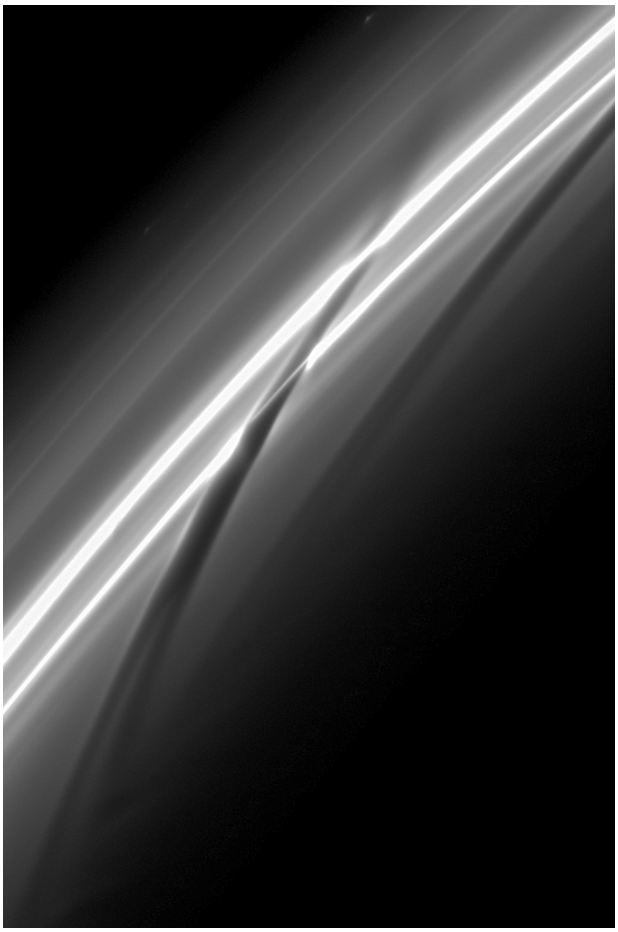

Figure 1.25 PIA10593. A cropped version of Cassini NAC image (N1610599806) of the F ring taken on 2009 January 14. The image covers $\sim 4°$ of longitude at the F ring core (upper bright component). The image illustrates the "channel" phase of the cycle along with the appearance of a residual ring in the bright component orbiting interior to the core. Note also the wedge of material in the channel at the lower right.

ner strand. This additional channel feature was predicted to exist on the basis of numerical simulations carried out by Chavez (2009) and only occurs when Prometheus and the F ring are near a maximum perturbation configuration. On the basis of the results of numerical integrations, Beurle et al. (2010) noted that the channels get wider with time. This agrees with the observations (see, e.g., Figure 2a of Beurle et al. (2010)). The widening can be understood in the context of the epicyclic diagram shown in Figure 1.24, where a similar widening with increasing time is seen. The perturbations in semi-major axis induced by the Prometheus encounter and the subsequent effects of Keplerian shear mean that once the "vertical" phase (evident after 3.5 orbital periods) has occurred the width of any individual gap is constantly widening.

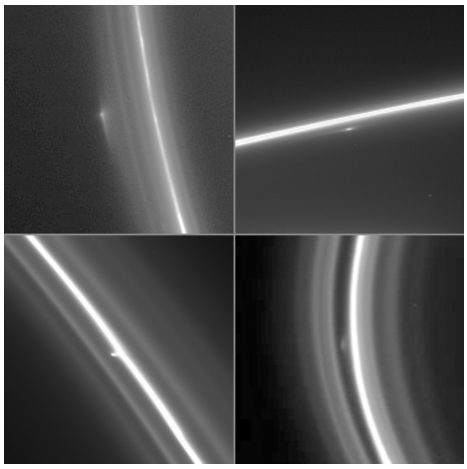

Figure 1.26 PIA07716. Four enhanced Cassini NAC images of objects near the F ring core. The upper two images are of S/2004 S 6 taken on 2005 June 21 and June 25 on opposite sides of the F ring core. At the time of initial release (September 2005) the object in the lower left image (taken on 2005 August 3) was thought to be S/2004 S 3 but now it and the object in the lower right image (taken on 2005 April 13) are thought to be examples of "mini-jets" caused by small moonlets undergoing low velocity (~ 1 ms^{-1}) collisions with the core.

1.7 Evidence for moonlets

Analyzing data from the Pioneer 11 charged particle experiments, Cuzzi and Burns (1988) attributed two of the five detected depletions of 7 MeV electrons to clumps of low optical depth ($\tau \sim 10^{-4}$–10^{-3}) material in the region between the orbits of Prometheus and Pandora. They envisaged that this was evidence for ejecta clouds from a belt of 0.1–10 km colliding moonlets; they also suggested that the F ring itself had been produced from a collision between the larger members of this group. A series of observations obtained during the May, August, and November 1995 ring-plane crossings (Bosh and Rivkin, 1996; Nicholson et al., 1996; Roddier et al., 2000; McGhee et al., 2001) led to the discovery of several bright objects and arc-like features in the vicinity of the F ring, some of which were consistent with the features deduced by Cuzzi and Burns (1988). Showalter (1998) argued that many of the objects were likely to be transitory clumps associated with impact events. Indeed, an analysis of additional observations by Poulet et al. (2000b) attributed several of the ring-plane crossing detections to a population of ~ 100 m – 1 km-sized objects within the F ring. Barbara and Esposito (2002) modeled the possible accretion and disruption mechanism in the F ring as a Markov process. They suggested that localized bright features in the F ring were the result of disruptive collisions of ∼km-sized "rubble pile" moonlets within the ring. In his pre-Cassini analysis of the clumps in the Voyager images, Showalter (2004) concluded that even though many of the objects observed during the 1995 ring-plane crossing had been given preliminary designations as satellites, they were more likely to have been transient clumps in the F ring itself.

Images obtained from Cassini ISS in the first year of the Saturn orbit tour showed the presence of three objects orbiting close to the F ring core, which also received preliminary designations as S/2004 S 3, S/2004 S 4 and S/2004 S 6 (Porco et al., 2005). These had estimated diameters of ~ 5 km, and while S/2004 S 3 was observed to orbit beyond the outermost F ring strand, both S/2004 S 4 and S/2004 S 6 were detected interior to the orbit of the core. No characteristic wavelengths (see Eq. (1.8)) associated with any of these objects have ever been observed, and although it is believed that S/2004 S 3 and S/2004 S 4 are the same body (N. Cooper, private communication) no further detections were obtained, thereby confirming initial suspicions that they were temporary. Given that the discovery of S/2004 S 6 was at a phase angle of 151°, it might be natural to assume that it was composed primarily of dust. However, an object on an orbit consistent with that of S/2004 S 6 was believed to play a role in the production of a series of bright jets that were seen to form in late 2006 and early 2007 (see below and Murray et al. (2008)). The orbit for this object given in the Supplementary Information for Murray et al. (2008) had a semi-major axis of 140135 km (i.e. ~ 90 km less than that of the F ring core) and was such that it crossed that of the F ring once per orbit, albeit in projection only. That is, a differing inclination may have caused it to pass above or below the F ring core. The current status of S/2004 S 6 is unknown but, to date, this is still the best candidate for an identifiable object that collides with the F ring core. Cassini NAC images of several of these objects are shown in Figure 1.26.

Esposito et al. (2008) reported the results of stellar occultations of the F ring region observed by the Cassini UVIS instrument. A total of 13 events with near- or total extinction were detected with widths in the range 27 m to 9 km; all but one of these events occurred within 15 km of the F ring core. Shallow profiles led them to attribute the cause of 12 of these events to loose agglomerations of dust, but one particular event, nicknamed "Mittens", had a wide profile with sharp edges suggestive of an opaque moonlet (see Figure 1.27); it had a width of 600 m and was located 4.29 km outside the core. Esposito et al. (2008) estimated a population of 3×10^4 such objects in the F ring region based on one detection in 44 independent occultation cuts. Meinke et al. (2012) further identified and classified similar features. They found the size distribution of clumps to be comparably shallow, as seen in Figure 1.28.

The lack of 360° coverage of the F ring region at high (sub-km) resolution makes it difficult to use ISS observations to determine the existence and nature of any moonlet belt orbiting close to the F ring core. Clearly, with the advent of Cassini, it is possible to rule out the presence of previously undiscovered, solid ~ 10 km-sized satellites orbiting close to the core because the extensive coverage at medium resolution (~ 10 km pixel^{-1}) means that such objects would have been detected by now. However, this does not rule out a similar population orbiting within the core itself (width ~ 40 km; see Section 1.2 above), provided there is both a lack of nearby ring material in which to leave a gravitational signature and yet sufficient material to provide a natural cover. Nevertheless, several different types of ISS observations provide strong evidence for moonlet populations.

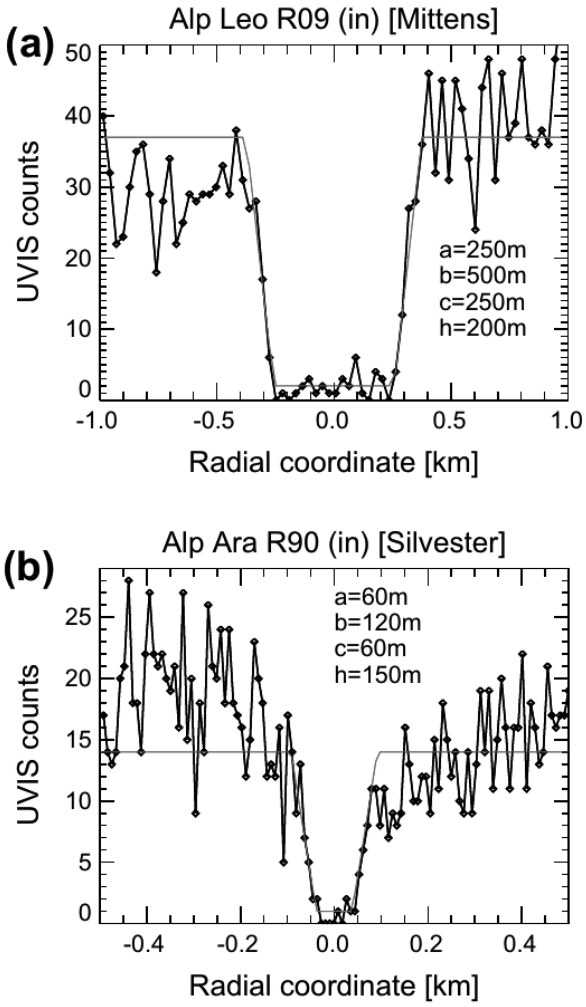

Figure 1.27 Cassini UVIS detected two events that are suggestive of opaque moonlets, nicknamed "'Mittens" and "Silvester". From Meinke et al. (2012).

Murray et al. (2008) pointed out the existence of "fan" structures at various locations in the core. These consist of a superimposed sequence of dark channels in any background dust, each appearing to emanate from a unique, bright point close to the core. The radiating pattern has the appearance of a fan (see Figure 1.29 for an example). Murray et al. (2008) showed how the presence of a fan is indicative of the perturbing effect of an embedded moonlet with a relative eccentricity (see, for example, Namouni (1999)) with respect to the core. The structure itself varies in a periodic manner on a timescale of an orbital period such that the fan appears and then disappears as part of its cycle (see Figs. 3a and 3b in Murray et al. (2008) for an observed example of this within the core). The effects of embedded satellites on rings in general and the mechanism of fan formation in particular

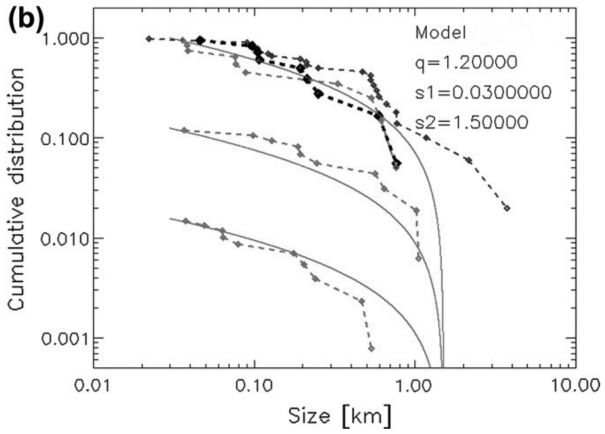

Figure 1.28 Inferred size distribution of detected clumps (upper two sets of black points). Shown for comparison are various surrogate size distributions (grey). From Meinke et al. (2012).

Figure 1.29 A 12° longitudinal section of the reprojected Cassini NAC image (N1571964006) shown in Figure 1.4b taken on 2007 October 25 showing the existence of two fan structures in the bright core $\sim 7°$ apart, each indicative of the presence of an embedded moonlet. The larger, in the background channels, were produced by a recent passage of Prometheus. The offset between the two sets of channels is probably a consequence of different eccentricities and peripases between the core and the inner strand. The reprojection is between inertial longitudes of 83° and 95° (compared to 82.31° and 100.54° in the original image) while the radial distance is between 140000 km and 140400 km.

have been studied in detail by Williams (2009). Noting the tendency for fan structures to appear at the edges of core channels produced by a recent Prometheus passage, Beurle et al. (2010) suggested that it was the perturbing action of Prometheus that triggered the formation of objects in the core; the post-encounter perturbed ring particles move on orbits such that the maximum surface density at one part of the cycle coincided with minimum relative velocity. Any objects that formed in this favorable environment would retain their perturbed orbital elements and start to perturb surrounding ring material, giving rise to the fan structures. Therefore, observations of these structures provide evidence for the existence and perhaps even local formation of embedded moonlets in the F ring core.

The existence of the jet structures emanating from the F ring core (see Section 1.2 above and Murray et al. (2008)) is another indication of the presence of a largely unseen population of moonlets in the region. In the image mosaics (similar to that in Figure 1.6) from late 2006 and early 2007 studied by Murray et al. (2008), the most prominent sequence of jets was clearly associated with the crossing of the core by an object identified as S/2004 S 6; other jets could be seen forming and shearing in the same mosaics indicating that additional moonlets were colliding with the core. With a relative velocity of ~ 30 ms^{-1}, collisions of S/2004 S 6 with the core are sufficient to spread material over several hundred kilometres, consistent with the extent of the observed jets (Charnoz, 2009). Numerical modeling of the collisional process by Charnoz (2009) consisted of two scenarios: a cluster of particles impacting a solid object in the core, and a solid object impacting a cluster of particles in the core. Although Charnoz (2009) favored the former, Attree et al. (2017) pointed out that neither model agrees with observations. In fact, with the use of numerical simulations of collisional processes, Attree et al. (2017) demonstrated that a scenario in which both the embedded object and the colliding object are composed of clusters of material gives the best agreement with Cassini observations. This would imply that the impacting moonlets are not solid but perhaps loose agglomerations (such as the structures detected by Esposito et al. (2008) and Meinke et al. (2012)), indicative of a particular formation or evolutionary process. Inspection of the two images of S/2004 S 6 in the upper part of Figure 1.26 show an extended, elongated structure which is at least consistent with this hypothesis although further research is necessary to elucidate the nature of this object.

An analysis of Cassini NAC images by Attree et al. (2012) and Attree et al. (2014) showed the presence near the core of mostly linear features they named "mini-jets". They interpreted these as being the product of collisions between unseen moonlets and the F ring. In their initial survey they noted ~ 570 mini-jets with ~ 10 being visible near the core at any given time. In many ways these are similar to the jets discussed above and in Section 1.2, although they are shorter and less bright than the jets. The impact velocities are estimated to be at least an order of magnitude smaller, implying that the source impactors are moving on orbits that are more similar to that of the core. In a sequence of images centered on Prometheus, Attree et al. (2012) were able to follow the evolution of a single mini-jet for ~ 9 hours as it came into and moved across the field of view of the NAC due to its δa with respect to Prometheus. Figure 1.30 shows reprojected images of the mini-jet feature at three separate times over ~ 6 hours, together with a plot of an evolving set of model particles moving on their epicyclic orbits as the structure undergoes Keplerian shear. The particles in the simulation would have started at a single point when they received their individual perturbations following a collisional event. This

would have produced a range of semi-major axes and eccentricities, thereby defining the pre-determined epicyclic ellipses (each with axes in the ratio of 2:1) to be followed (see Murray and Dermott (1999) and the Chapter 2 by Hedman for a discussion of the guiding center approximation and epicyclic motion). A combination of the particles' motion around their epicycles and the fact that each path is undergoing a different rate of Keplerian shear will account for the lengthening of the mini-jet and its collapse towards the core. In principle it is possible for a mini-jet to survive its first collapse and to re-emerge to complete another cycle although this is difficult to see without extended observations of a specific mini-jet. A more complete survey of ~ 800 mini-jets was undertaken by Attree et al. (2014) in an attempt to place constraints on the moonlet population that produced them. They deduced that the population consisted of a few hundred objects with a radius $\lesssim 1$ km and orbits with semi-major axes within ± 100 km of the core but with the majority of objects lying within ± 20 km. The chaotic nature of this region and the frequent collisions suggest that such objects will not remain in this region permanently and so this strongly suggests that they must be regenerated.

Many of the observed characteristics of the mini-jets can be attributed to the fact that when a suite of objects on circular orbits receive impulses at a single place and time, the change in semi-major axis, Δa, is related to the change in eccentricity, Δe, by

$$\Delta a \approx a\,\Delta e\,, \tag{1.10}$$

where a is the semi-major axis of the orbit. This relation explains, for example, the similarity in the shape of the Δa and Δe plots shown in Figure 1.23, because the result is the same whether the perturbation arises from a collision or a gravitational "kick". Attree et al. (2017) carried out a detailed analysis of the role of collisions in the F ring, including numerical simulations of the collisional process. One surprising result was that, in the case of the major jets, $\Delta a > a\,\Delta e$, consistently. Given that the change in longitude of periapse, $\Delta\varpi$, is related to Δe by the relative eccentricity, one possibility is that any offsets in periapse are being reduced by a secular locking mechanism and so a lower $\Delta\varpi$ will mean a lower Δe than expected. However, this topic needs more research both in terms of observations and theory.

Attree et al. (2017) also concluded that, at any given time, there are similar numbers of jets and mini-jets visible in the ring. However, the lifetime of jets is an order of magnitude larger than that of mini-jets, and so on this basis they concluded there must be ten times as many smaller objects producing mini-jets as there are larger objects producing jets. Furthermore, the simulations suggested that the observed characteristics of the jets could only be explained if the impacting objects were already partially disrupted.

1.8 Dynamical environment

As has been shown above, there is now clear evidence of the role played by Prometheus in creating clumps in the F ring and how these clumps may evolve dynamically to undergo collisions with the core, thereby producing further material that, under the influence of Prometheus, can again form clumps as part of an on-going cycle. However, although Prometheus – and to a lesser extent Pandora – play a role in determining the structure of the F ring, their possible influence in confining the F ring is less clear. In the case of the ϵ ring of Uranus it is generally accepted that the satellites Cordelia and Ophelia provide an example of confinement of the narrow ring by the shepherding mechanism, with Cordelia (the inner satellite) having a 24:25 outer eccentric resonance with the inner edge and Ophelia (the outer satellite) having a 14:13 inner eccentric resonance with the outer edge (Porco and Goldreich, 1987). However, it is by no means clear that a similar mechanism operates at the F ring.

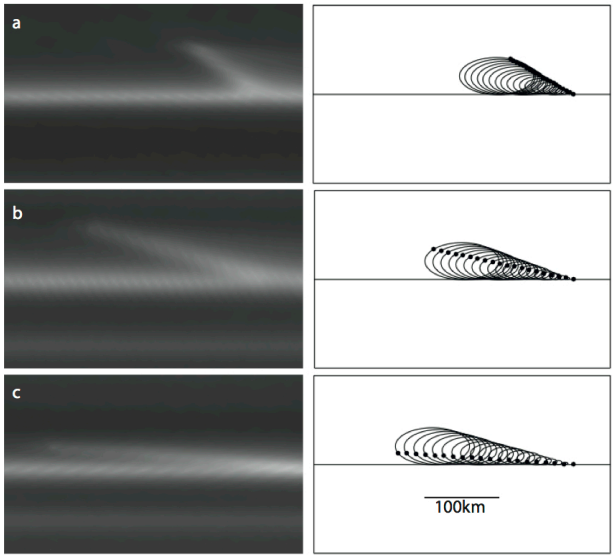

Figure 1.30 Left: Three reprojected images of the same linear feature (a mini-jet) evolving and collapsing to towards the F ring core. The images are (a) N1612002457, (b) N1612013501 and (c) N1612022286, all taken on 2009 January 30. The time interval between images is ~ 3 hours. Right: The equivalent epicyclic paths (the outlined ellipses) followed by particles (black dots) forming the material in the mini-jet. Each frame is to the same scale and covers a region of 400 × 200 km. Figure adapted from Attree et al. (2012).

Figure 1.31 shows the location in semi-major axis of all first-order resonances with known satellites in a 25 km-wide region close to the F ring core, together with the various determinations of the semi-major axis of the F ring core. Note that the separation of the first-order Prometheus resonances is ~ 8 km at this location while those of the first-order Pandora resonances is ~ 13 km. For the purpose of comparison, the approximate width of a first-order Prometheus Lindblad resonance in this region is ~ 7 km using Eq. (10.24) from Murray and Dermott (1999); the same calculation for Pandora gives a width of ~ 6 km. Labels with the letters A, B, and C in Figure 1.31 denote the semi-major axis determinations of Albers et al. (2012), Bosh et al. (2002) and Cooper

et al. (2013), respectively. In the latter case the numbers denote the orbit fits: C1 to C10 were for individual core segments and therefore represent localized orbit determinations, while C11 denotes an orbit fit using the data points from all segments. Fit C12 only makes use of measurements that are at least 2° ahead of Prometheus in order to minimize any possible bias from recently perturbed ring material. Note that the orbit fit given in Table 1.1 is Fit C11.

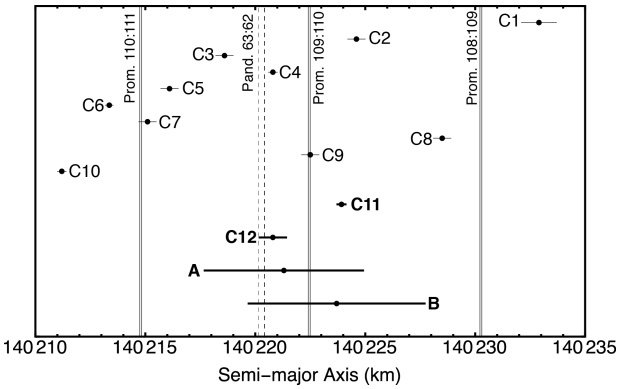

Figure 1.31 The location of all first-order mean motion resonances located between 140210 and 140235 km compared to the calculated semi-major axes of the F ring's core. The semi-major axes and mean motion of Prometheus and Pandora were taken to be 139377.9 km and 141712.5 km, respectively. The three Prometheus resonances (110:111, 111:112 and 112:113) are denoted by three sets of vertical, solid, double lines and the $p + 1 : p$ values are indicated. The single Pandora resonance, 63:62, is denoted by the vertical, dashed double line. Note that the corotation and Lindblad resonance that make up each line pair are typically $\sim$ 0.1–0.2 km apart. The labels B and A denote the F ring orbit calculated by Bosh et al. (2002) and Albers et al. (2012), respectively. The labels C1 to C12 denote fits 1 to 12 respectively in table 3 of Cooper et al. (2013). C11 is the fit used in Table 1.1 above.

The spread in the individual core segment fits labeled C1 to C10 in Figure 1.31 shows how localized change in semi-major axis can be affected by Prometheus. Note also that the spread in semi-major axis is consistent with that expected based on Figure 1.23 as well as the clump distribution shown in Figure 1.8 and the extended club distribution shown in Figure 1.17. Therefore, on this basis the F ring as observed by the Cassini ISS has no unique semi-major axis even though the C11 and C12 orbit fits are consistent with the data derived from occultation studies (A and B). Nevertheless, the ring continues to precess uniformly as though it had a unique semi-major axis; thus the pre-Cassini fit by Bosh et al. (2002) was only superseded recently, though we do not know why uniform precession occurs in the first place. The likely reasons involve self-gravity and/or collisions, but the lack of any reliable determination of the mass of the F ring makes it difficult to constrain precession models.

The fact that the resonance widths are $\sim$ 6–7 km compared with a separation of $\sim$ 8 km for the Prometheus resonances means that particle orbits in the immediate vicinity of the core are likely to be undergoing chaotic evolution. Furthermore, Prometheus and Pandora perturb each other chaotically primarily by means of four overlapping 121:118 mutual resonances, (Goldreich and Rappaport, 2003a,b) though the situation is made even more complicated by the Janus-Epimetheus swap and the existence of the Mimas 3:2 resonance close to the orbit of Pandora (Cooper and Murray, 2004). Therefore it is not surprising that various authors have undertaken numerical studies to investigate the stabil-

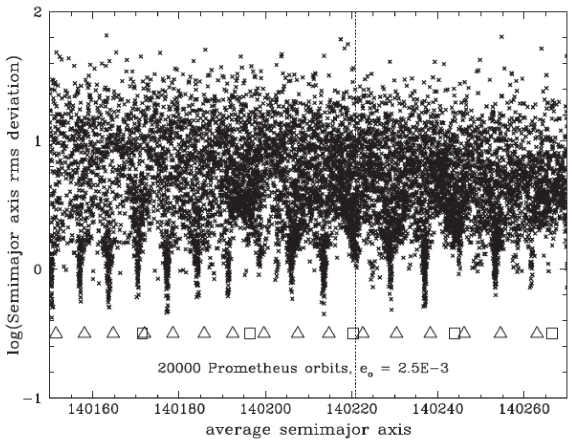

Figure 1.32 The results of numerical integrations of 12000 test particles for 2×10^4 Prometheus orbits in the vicinity of the F ring carried out by Cuzzi et al. (2014a). The dotted line denotes the average semi-major axis of the Albers et al. (2012) fit and Cooper et al. (2013), fit 12. Triangles denote the location of Prometheus' outer Lindblad resonances and squares denote the location of Pandora's inner Lindblad resonances. From Cuzzi et al. (2014a).

ity of ring particle orbits in this region (see, e.g. Winter et al. (2007), Winter et al. (2010)).

Cuzzi et al. (2014a) have looked at the long-term stability of particle orbits in the vicinity of the F ring by means of numerical integrations and have devised a novel mechanism to explain the results. By carrying out extensive integrations of test particles they found, unsurprisingly, that the orbits in this region are chaotic. However, by measuring the root mean square (rms) deviation in the particles' semimajor axes, they showed that there were discrete minima at locations near but just interior to the first-order Lindblad resonances with Prometheus (see Figure 1.32). Cuzzi et al. (2014a) refer to these as "narrow zones of higher stability". For example, whereas typical rms values were ~ 30 km, at the resonant locations the values were < 1 km. Exceptions occurred where there was a Pandora resonance; in these cases the rms value was larger. Both Cooper et al. (2013) and Cuzzi et al. (2014a) noted that the approximate empirical relation

$$n_{\rm P} - n_{\rm F} \approx 2\dot{\varpi}_{\rm F} \tag{1.11}$$

appears to hold in this region, where n is the mean motion, ϖ is the longitude of perichrone and the subscripts P and F refer to the Prometheus and the F ring respectively. Cooper et al. (2013) noted that, in practical terms, this means that if a particle is at its perichrone/apochrone when it encounters Prometheus then it will be at its apochrone/perichrone when it next encounters Prometheus. Therefore there will be a tendency for any change in semi-major axis acquired at one encounter to be canceled by an equal and approximately opposite change at the next encounter. The repeated configurations afforded by resonance mean that this behavior occurs in the F ring region. In fact, Cuzzi et al. (2014a) observed exactly this behavior in their numerical integrations and used a toy model together with a more detailed analysis to examine the mechanism. They referred to these as "antiresonances" because of their presumed ability to counteract the possible diffusive effect of resonance. In the F ring region these occur at intervals of $\sim 7-8$ km and Cuzzi et al. (2014a) claimed that the F ring core is located at one of the relatively stable zones caused by these antiresonances, although they acknowledge that their mechanismm cannot counteract the effects of the large ± 20 km changes in semimajor axis that can be induced by Prometheus when it is at its apoapse.

However, in a follow-up paper (see Cuzzi et al. (2014b) and Chapter 3 of this volume) the authors use an analysis of Cassini Radio Science Subsystem (RSS) occultation data (Marouf et al. (2010)) to claim that there is evidence that the detected ring material is clustered at specific locations consistent with what would be expected from a corotation resonance. Furthermore they identified a specific resonance, the Prometheus 109:110 outer corotation eccentric resonance (see Figure 1.31), as the best candidate to fit the data and pointed out that its location, uniquely in this entire region, is almost coincident with that of one of their antiresonance locations. However, it is worth pointing out that the Prometheus outer Lindblad resonances are located close by, only ~ 100 m exterior to the corotation resonances. In integrations of test particles using successively lower values of J_2, J_4, and J_6, Cuzzi et al. (2014a) noted (Figure 9 of their paper) that the location of the "narrow zones of higher stability" shifted to the outside of the resonant location as the values decreased. This could be consistent with relative changes in the location of the two types of resonance. In any case the fact remains that the F ring as observed by Cassini ISS, VIMS and UVIS does not have a well-defined semimajor axis although this may not be the case for the RSS F ring. The near-superposition of the Lindblad and corotation resonances suggests that it may be possible to explain the numerical results using a limiting form of the CoraLin model (see El Moutamid et al. (2014)), which approximates the dynamics of a system involving both types of resonances and two orbiting masses; in the case of interest here, the mass of one of the mutual perturbers goes to zero.

There is also the possibility that the F ring seen in ISS, VIMS, and UVIS data is not where the mass resides. Murray et al. (2008) reported the existence of a narrow, noncontinuous component of the F ring with a radial width ~ 1 km. The F ring detected in the Cassini RSS occultation experiment as reported by Marouf et al. (2010) was ~ 100 m wide. The relationship between the rings observed by the optical remote sensing instruments (ISS, UVIS, and VIMS) and that detected by the RSS is not clear, and this is an active area of research. The whole question of the ring's confinement (or lack thereof) needs to be resolved, as does the mechanism that maintains uniform precession. There is also the problem of how the F ring fits into models for the origin of the main rings and satellites (see, e.g., Crida and Charnoz (2012)).

1.9 Conclusions

Despite the undoubted new insights achieved as a result of the Cassini observations, in many ways the F ring remains as enigmatic today as when it was first glimpsed by the Pioneer 11 spacecraft in 1979. It is perhaps the most dynamic and variable of all the rings, with changes being observed on timescales ranging from hours to decades. The Cassini observations have clarified the role of Prometheus in producing the regular streamer-channel structures and, thereby, the associated clumps. The latter, in turn, give rise to a source of new objects to collide with the core and produce the observed jets. However, the differences between the Voyager and Cassini observations are difficult to account for, and there are too few constraints on the population of colliding objects. There are more fundamental problems as well. Despite all the localized disruption and the clearly chaotic dynamical nature of the entire region, the ring continues to maintain a reasonably coherent structure and precesses uniformly. This may be due to a combination of collisions and self-gravity, but this is difficult to prove when the total mass of the system is essentially unknown. Although recent progress has been made in understanding the location and relative stability of the ring, its origin and future are still unclear.

1.10 Acknowledgments

We thank Nicole Albers and Matt Hedman for providing several diagrams. We are grateful to Tracy Becker, Jeff Cuzzi and Matt Tiscareno for providing thorough reviews of our original draft. Carl Murray was supported by the UK Science and Technology Facilities Council (Grant No. ST/F007566/1) and is grateful to them for financial assistance.

REFERENCES

Albers, Nicole, Sremčević, Miodrag, Colwell, Joshua E., and Esposito, Larry W. 2012. Saturn's F ring as seen by Cassini UVIS: Kinematics and statistics. *Icarus*, **217**(Jan.), 367–388.

Attree, N. O., Murray, C. D., Cooper, N. J., and Williams, G. A. 2012. Detection of Low-velocity Collisions in Saturn's F Ring. *The Astrophysical Journal Letters*, **755**(Aug.), L27.

Attree, N. O., Murray, C. D., Williams, G. A., and Cooper, N. J. 2014. A Survey of Low-Velocity Collisional Features in Saturn's F Ring. *Icarus*, **227**, 56–66.

Attree, N. O., Murray, C. D., Cooper, N. J., and Williams, G. A. 2017. The morphology and dynamics of Saturn's F ring: II. The role of collisions. *Icarus*.

Barbara, John M., and Esposito, Larry W. 2002. Moonlet collisions and the effects of tidally modified accretion in Saturn's F ring. *Icarus*, **160**(Nov.), 161–171.

Becker, Tracy M. 2016 (Dec.). *Saturn's Rings: Measuring Particle Size Distributions Using Cassini UVIS Occultation Data*. Ph.D., University of Central Florida, Orlando, FL.

Beurle, K., Murray, C. D., Williams, G. A., Evans, M. W., Cooper, N. J., and Agnor, C. B. 2010. Direct evidence for gravitational instability and moonlet formation in Saturn's rings. *The Astrophysical Journal*, **718**(Aug.), L176–180.

Borderies, N., Goldreich, P., and Tremaine, S. 1983. The variations in eccentricity and apse precession rate of a narrow ring perturbed by a close satellite. *Icarus*, **53**(Jan.), 84–89.

Bosh, A. S., Olkin, C. B., French, R. G., and Nicholson, P. D. 2002. Saturn's F ring: Kinematics and particle sizes from stellar occultation studies. *Icarus*, **157**(May), 57–75.

Bosh, Amanda S., and Rivkin, Andrew S. 1996. Observations of Saturn's inner satellites during the May 1995 ring-plane crossing. *Science*, **272**(Apr.), 518–521.

Burns, J. A., Showalter, M. R., and Morfill, G. E. 1984. The ethereal rings of Jupiter and Saturn. Pages 200–272 of: Greenberg, R., and Brahic, A. (eds), *Planetary Rings*. Tucson, AZ: University of Arizona Press.

Chandrasekhar, S. 1960. *Radiative Transfer*. New York, NY: Dover Publications, Inc.

Charnoz, S., Porco, C. C., Déau, E., Brahic, A., Spitale, J. N., Bacques, G., and Baillie, K. 2005. Cassini discovers a kinematic spiral ring around Saturn. *Science*, **310**(Nov.), 1300–1304.

Charnoz, Sébastien. 2009. Physical collisions of moonlets and clumps with the Saturn's F-ring core. *Icarus*, **201**(1), 191–197.

Chavez, Carlos E. 2009. Appearance of Saturn's F ring azimuthal channels for the anti-alignment configuration between the ring and Prometheus. *Icarus*, **203**(Sept.), 233–237.

Christiansen, C. 1884. Untersuchungen über die optischen Eigenschaften von fein vertheilten Körpern. *Annalen der Physik*, **259**, 298–306.

Christiansen, C. 1885. Untersuchungen über die optischen Eigenschaften von fein vertheilten Körpern. *Annalen der Physik*, **260**, 439–446.

Cooper, N. J., and Murray, C. D. 2004. Dynamical influences on the orbits of Prometheus and Pandora. *Astronomical Journal*, **127**, 1204–1217.

Cooper, N. J., Murray, C. D., and Williams, G. A. 2013. Local Variability in the Orbit of Saturn's F Ring. *Astronomical Journal*, **145**(6), 161.

Cooper, N. J., Renner, S., Murray, C. D., and Evans, M. W. 2015. Saturns inner satellites: Orbits, masses, and the chaotic motion of Atlas from new Cassini imaging observations. *Astronomical Journal*, **149**(1), 18.

Crida, A., and Charnoz, S. 2012. Formation of Regular Satellites from Ancient Massive Rings in the Solar System. *Science*, **338**, 1196.

Cuzzi, J. N. 1985. Rings of Uranus - Not so thick, not so black. *Icarus*, **63**(Aug.), 312–316.

Cuzzi, J. N., and Burns, J. A. 1988. Charged particle depletion surrounding Saturn's F ring - Evidence for a moonlet belt? *Icarus*, **74**(May), 284–324.

Cuzzi, J. N., Whizin, A. D., Hogan, R. C., Dobrovolskis, A. R., Dones, L., Showalter, M. R., Colwell, J. E., and Scargle, J. D. 2014a. Saturn's F Ring core: Calm in the midst of chaos. *Icarus*, **232**(Apr.), 157–175.

Cuzzi, J. N., Marouf, E. A., French, R. C., and Jacobson, R. 2014b (August). Saturn's F ring core: Calm in the midst of chaos; Part 2. In: Esposito, L. W. (ed), *Planetray Rings Summer Workshop*.

Cuzzi, Jeff, Clark, Roger, Filacchione, Gianrico, French, Richard, Johnson, Robert, Marouf, Essam, and Spilker, Linda. 2009. Ring Particle Composition and Size Distribution. Page 459 of: *Saturn from Cassini-Huygens*.

Dermott, S. F., Gold, T., and Sinclair, A. T. 1979. The rings of Uranus – Nature and origin. *Astronomical Journal*, **84**(August), 1225–1232.

Dones, Luke, Cuzzi, Jeffrey N., and Showalter, Mark R. 1993. Voyager photometry of Saturn's A ring. *Icarus*, **105**(Sept.), 184–215.

El Moutamid, Maryame, Sicardy, Bruno, and Renner, Stéfan. 2014. Coupling between corotation and Lindblad resonances in the presence of secular precession rates. *Celestial Mechanics and Dynamical Astronomy*, **118**, 235–252.

Elliot, J. L., French, R. G., Meech, K. J., and Elias, J. H. 1984. Structure of the Uranian rings. I - Square-well model and particle-size constraints. *The Astronomical Journal*, **89**(Oct.), 1587–1603.

Esposito, Larry W., Meinke, Bonnie K., Colwell, Joshua E., Nicholson, Philip D., and Hedman, Matthew M. 2008. Moonlets and clumps in Saturn's F ring. *Icarus*, **194**(Mar.), 278–289.

French, Richard G., Nicholson, Philip D., Porco, Carolyn C., and Marouf, Essam A. 1991. Dynamics and structure of the Uranian rings. Pages 327–409 of: Bergstralh, J. T., Miner, E. D., and Matthews, M. S. (eds), *Uranus*. Tucson, AZ: University of Arizona Press.

French, Robert S., Showalter, Mark R., Sfair, Rafael, Argüelles, Carlos A., Pajuelo, Myriam, Becerra, Patricio, Hedman, Matthew M., and Nicholson, Philip D. 2012. The brightening of Saturn's F ring. *Icarus*, **219**(1), 181–193.

French, Robert S., Hicks, Shannon K., Showalter, Mark R., Antonsen, Adrienne K., and Packard, Douglas R. 2014. Analysis of clumps in Saturn's F ring from Voyager and Cassini. *Icarus*, **241**(Oct.), 200–220.

Gehrels, T., Baker, L. R., Beshore, E., Blenman, C., Burke, J. J., Castillo, N. D., Dacosta, B., Degewij, J., Doose, L. R., Fountain, J. W., Gotobed, J., Kenknight, C. E., Kingston, R., McLaughlin, G., McMillan, R., Murphy, R., Smith, P. H., Stoll, C. P., Strickland, R. N., Tomasko, M. G., Wijesinghe, M. P., Coffeen, D. L., and Esposito, L. W. 1980. Imaging photopolarimeter on Pioneer Saturn. *Science*, **207**(4429), 434–439.

Giuliatti Winter, S. 1994 (August). *The dynamics of Saturn's F ring*. Ph.D. thesis, Queen Mary and Westfield College, University of London.

Goldreich, Peter, and Rappaport, Nicole. 2003a. Chaotic motions of prometheus and pandora. *Icarus*, **162**(Apr.), 391–399.

Goldreich, Peter, and Rappaport, Nicole. 2003b. Origin of chaos in the Prometheus-Pandora system. *Icarus*, **166**(Dec.), 320–327.

Grun, E., Morfill, G. E., and Mendis, D. A. 1984. Dust-magnetosphere interactions. Pages 275–332 of: *Planetary rings*. Tucson, AZ: University of Arizona Press.

Hansen, J. E., and Travis, L. D. 1974. Light scattering in planetary atmospheres. *Space Science Reviews*, **16**(Oct.), 527–610.

Hedman, M. M., Nicholson, P. D, Showalter, M. R., Brown, R. H., Buratti, B. J., Clark, R. N., Baines, K., and Sotin, C. 2011. The Christiansen Effect in Saturn's narrow dusty rings and the spectral identification of clumps in the F ring. *Icarus*, **215**(Oct.), 695–711.

Jacobson, R. A., Spitale, J., Porco, C. C., Beurle, K., Cooper, N. J., Evans, M. W., and Murray, C. D. 2008. Revised orbits of Saturn's small inner satellites. *Astronomical Journal*, **135**(1), 261–263.

Kolvoord, Robert A., and Burns, Joseph A. 1992. Three-dimensional perturbations of particles in a narrow planetary ring. *Icarus*, **95**(Feb.), 253–264.

Lam, Wai Fun. 2014 (April). *Clumping features in Saturn's F ring*. M.Phil. thesis, Queen Mary University of London.

Lane, A. L., Hord, C. W., West, R. A., Esposito, L. W., Coffeen, D. L., Sato, M., Simmons, K. E., Pomphrey, R. B., and Morris, R. B. 1982. Photopolarimetry from Voyager 2 – Preliminary results on Saturn, Titan, and the rings. *Science*, **215**(January), 537–543.

Marouf, E. A., Tyler, G. L., and Rosen, P. A. 1986. Profiling Saturn's rings by radio occultation. *Icarus*, **68**(Oct.), 120–166.

Marouf, Essam A., Wong, K., French, R., Rappaport, N., and McGhee, C. 2010 (Oct.). The Discontinuous Core of Saturn's F-Ring and Orbit Model. vol. 42.

McGhee, Colleen A., Nicholson, Philip D., French, Richard G., and Hall, Katherine J. 2001. HST observations of Saturnian satellites during the 1995 ring plane crossings. *Icarus*, **152**(Aug.), 282–315.

Meinke, Bonnie K., Esposito, Larry W., Albers, Nicole, and Sremčević, Miodrag. 2012. Classification of F ring features observed in Cassini UVIS occultations. *Icarus*, **218**(Mar.), 545–554.

Murray, Carl D. 1994. Planetary ring dynamics. *Philosophical Transactions of the Royal Society of London*, **349**, 335–344.

Murray, Carl D., and Dermott, Stanley F. 1999. *Solar system dynamics*. Cambridge University Press.

Murray, Carl D., and Giuliatti Winter, Silvia M. 1996. Periodic collisions between the moon Prometheus and Saturn's F ring. *Nature*, **380**(Mar.), 139–141.

Murray, Carl D., Gordon, Mitchell K., and Giuliatti Winter, Silvia M. 1997. Unraveling the strands of Saturn's F ring. *Icarus*, **129**(Oct.), 304–316.

Murray, Carl D., Chavez, Carlos, Beurle, Kevin, Cooper, Nick, Evans, Michael W., Burns, Joseph A., and Porco, Carolyn C. 2005. How Prometheus creates structure in Saturn's F ring. *Nature*, **437**(Oct.), 1326–1329.

Murray, Carl D., Beurle, Kevin, Cooper, Nicholas J., Evans, Michael W., Williams, Gareth A., and Charnoz, Sbastien. 2008. The determination of the structure of Saturn's F ring by nearby moonlets. *Nature*, **453**(June), 739–744.

Murray, Carl D., Cooper, Nicholas J., Williams, Gareth A., and Attree, N. O. 2017. The morphology and dynamics of Saturn's F ring. I: Gravitational effects. *Icarus*.

Namouni, F. 1999. Secular Interactions of Coorbiting Objects. *Icarus*, **137**(2), 293–314.

Nicholson, Philip D., Showalter, Mark R., Dones, Luke, French, Richard G., Larson, Stephen M., Lissauer, Jack J., McGhee, Colleen A., Seitzer, Patrick, Sicardy, Bruno, and Danielson, G. Edward. 1996. Observations of Saturn's ring-plane crossings in August and November 1995. *Science*, **272**(Apr.), 509–515.

Ockert, Maureen E., Cuzzi, Jeffrey N., Porco, Carolyn C., and Johnson, Torrence V. 1987. Uranian ring photometry - Results from Voyager 2. *Journal of Geophysical Research*, **92**(Dec.), 14969–14978.

Pollack, J. B., and Cuzzi, J. N. 1980. Scattering by nonspherical particles of size comparable to wavelength - A new semi-empirical theory and its application to tropospheric aerosols. *Journal of Atmospheric Sciences*, **37**, 868–881.

Porco, C. C., Baker, E., Barbara, J., Beurle, K., Brahic, A., Burns, J. A., Charnoz, S., Cooper, N., Dawson, D. D., Del Genio, A. D., Denk, T., Dones, L., Dyudina, U., Evans, M. W., Giese, B., Grazier, K., Helfenstein, P., Ingersoll, A. P., Jacobson, R. A., Johnson, T. V., McEwen, A., Murray, C. D., Neukum, G., Owen, W. M., Perry, J., Roatsch, T., Spitale, J., Squyres, S., Thomas, P., Tiscareno, M., Turtle, E., Vasavada, A. R., Veverka, J., Wagner, R., and West, R. 2005. Cassini imaging science: Initial results on Saturn's rings and small satellites. *Science*, **307**(5713), 1226–1236.

Porco, Carolyn C., and Goldreich, P. 1987. Shepherding of the Uranian rings. I. Kinematics. *Astronomical Journal*, **93**, 724–737.

Porco, Carolyn C., West, Robert A., Squyres, Steven, McEwen, Alfred, Thomas, Peter, Murray, Carl D., Del Genio, Anthony, Ingersoll, Andrew P., Johnson, Torrence V., Neukum, Gerhard, Veverka, Joseph, Dones, Luke, Brahic, Andre, Burns, Joseph A., Haemmerle, Vance, Knowles, Benjamin, Dawson, Douglas, Roatsch, Thomas, Beurle, Kevin, and Owen, William. 2004. Cassini Imaging Science: Instrument Characteristics And Anticipated Scientific Investigations At Saturn. *Space Science Reviews*, **115**(1–4), 363–497.

Poulet, FranÃ§ois, Sicardy, Bruno, Dumas, Christophe, Jorda, Laurent, and TiphÃne, Didier. 2000a. The Crossings of Saturn Ring Plane by the Earth in 1995: Ring Thickness. *Icarus*, **145**(May), 147–165.

Poulet, FranÃ§ois, Sicardy, Bruno, Nicholson, Philip D., Karkoschka, Erich, and Caldwell, John. 2000b. Saturn's ring-plane crossings of August and November 1995: A model for the new F-ring objects. *Icarus*, **144**(Mar.), 135–148.

Roddier, F., Roddier, C., Brahic, A., Dumas, C., Graves, J. E., Northcott, M. J., and Owen, T. 2000. Adaptive Optics Observations of Saturn's Ring Plane Crossing in August 1995. *Icarus*, **143**(Feb.), 299–307.

Scharringhausen, Britt R., and Nicholson, Philip D. 2013. The vertical structure of the F ring of Saturn from ring-plane crossings. *Icarus*, **226**(Nov.), 1275–1293.

Showalter, M. R., and Burns, J. A. 1982. A numerical study of Saturn's F-ring. *Icarus*, **52**(Dec.), 526–544.

Showalter, M. R., Burns, J. A., Cuzzi, J. N., and Pollack, J. B. 1987. Jupiter's ring system - New results on structure and particle properties. *Icarus*, **69**(Mar.), 458–498.

Showalter, Mark R. 1998. Detection of centemeter-sized meteoroid impact events in Saturn's F ring. *Science*, **282**(November), 1099–1102.

Showalter, Mark R. 2004. Disentangling Saturn's F ring. I. Clump orbits and lifetimes. *Icarus*, **171**(Oct.), 356–371.

Showalter, Mark R., Pollack, James B., Ockert, Maureen E., Doyle, Laurance R., and Dalton, J. B. 1992. A photometric study of Saturn's F ring. *Icarus*, **100**(Dec.), 394–411.

Simpson, J. A., Bastian, T. S., Chenette, D. L., Lentz, G. A., McKibben, R. B., Pyle, K. R., and Tuzzolino, A. J. 1980. Saturnian trapped radiation and its absorption by satellites and rings – The first results from Pioneer 11. *Science*, **207**(January), 411–415.

Smith, B. A., Soderblom, L., Beebe, R. F., Boyce, J. M., Briggs, G., Bunker, A., Collins, S. A., Hansen, C., Johnson, T. V., Mitchell, J. L., Terrile, R. J., Carr, M. H., Cook, A. F., Cuzzi, J. N., Pollack, J. B., Danielson, G. E., Ingersoll, A. P., Davies, M. E., Hunt, G. E., Masursky, H., Shoemaker, E. M., Morrison, D., Owen, T., Sagan, C., Veverka, J., Strom, R., and Suomi, V. E. 1981. Encounter with Saturn – Voyager 1 imaging science results. *Science*, **212**(April), 163–191.

Smith, B. A., Soderblom, L., Batson, R. M., Bridges, P. M., Inge, J. L., Masursky, H., Shoemaker, E., Beebe, R. F., Boyce, J., Briggs, G., Bunker, A., Collins, S. A., Hansen, C., Johnson, T. V., Mitchell, J. L., Terrile, R. J., Cook, A. F., Cuzzi, J. N., Pollack, J. B., Danielson, G. E., Ingersoll, A. P., Davies, M. E., Hunt, G. E., Morrison, D., Owen, T., Sagan, C., Veverka, J., Strom, R., and Suomi, V. E. 1982. A new look at the Saturn system - The Voyager 2 images. *Science*, **215**(January), 504–537.

Synnott, S. P., Peters, C. F., Smith, B. A., and Morabito, L. A. 1981. Orbits of the small satellites of Saturn. *Science*, **212**(April), 191–192.

Synnott, S. P., Terrile, R. J., Jacobson, R. A., and Smith, B. A. 1983. Orbits of Saturn's F ring and its shepherding satellites. *Icarus*, **53**(Jan.), 156–158.

Tyler, G. L., Marouf, E. A., Simpson, R. A., Zebker, H. A., and Eshleman, V. R. 1983. The microwave opacity of Saturn's rings at wavelengths of 3.6 and 13 CM from Voyager 1 radio occultation. *Icarus*, **54**(May), 160–188.

Vahidinia, Sanaz, Cuzzi, Jeffrey N., Hedman, Matt, Draine, Bruce, Clark, Roger N., Roush, Ted, Filacchione, Gianrico, Nicholson, Philip D., Brown, Robert H., Buratti, Bonnie, and Sotin, Christophe. 2011. Saturn's F ring grains: Aggregates made of crystalline water ice. *Icarus*, **215**(Oct.), 682–694.

Williams, Gareth A. 2009. *The three-body problem applied to close ring-satellite encounters*. Ph.D. thesis, Queen Mary University of London.

Winter, O. C., MourÃo, D. C., Giuliatti Winter, S. M., Spahn, F., and da Cruz, C. 2007. Moonlets wandering on a leash-ring. *Monthly Notices of the Royal Astronomical Society*, **380**(Sept.), L54–57.

Winter, O. C., MourÃo, D. C., and Giuliatti Winter, S. M. 2010. Short Lyapunov time: a method for identifying confined chaos. *Astronomy and Astrophysics*, **523**.